Mineralogical Magazine (2024), 1–21
doi:10.1180/mgm.2024.41

Article

Kobellite homologues from the Boliden Au–Cu–(As) deposit, Sweden: jigsaw patterning via nanoscale intergrowths in chessboard structures

Nanominerals and mineral nanoparticles – thematic issue

Cristiana L. Ciobanu[1], Ashley D. Slattery[2], Nigel J. Cook[1], Benjamin P. Wade[2], Kathy Ehrig[3,1], Thomas Wagner[4] and Wenyuan Liu[5]

[1]School of Chemical Engineering, The University of Adelaide, Adelaide, SA 5005, Australia; [2]Adelaide Microscopy, The University of Adelaide, Adelaide, SA 5005, Australia; [3]BHP Olympic Dam, 10 Franklin Street, Adelaide SA 5000, Australia; [4]Institute of Applied Mineralogy and Economic Geology, RWTH Aachen University, Germany; and [5]Zijin School of Geology and Mining, Fuzhou University, Fuzhou 350108, China

Abstract

Sulfosalt assemblages in a specimen from the Boliden Au–Cu–(As) deposit in northern Sweden, comprise micrometre to nanometre scale intergrowths of Se-rich izoklakeite and tintinaite with average formulae and calculated homologue number (N) given as: $(Cu_{1.88}Fe_{0.18})_{2.06}(Pb_{22.92}Ag_{1.47}Cd_{0.01}Zn_{0.01})_{24.41}(Sb_{13.12}Bi_{8.69})_{21.8}(S_{50.19}Se_{6.43}Te_{0.12})_{56.73,}$ $N = 3.83$, and $(Cu_{1.31}Fe_{0.74})_{2.05}(Pb_{10.58}Ag_{0.18}Cd_{0.05}Zn_{0.02})_{10.83}(Sb_{10.2}Bi_{5.23})_{15.43}(S_{32.22}Se_{2.46})_{34.7}$, $N = 2.05$, respectively. Tintinaite coexists with (Bi, Se)-rich jamesonite. High-angle annular dark field scanning transmission electron microscopy (HAADF STEM) imaging reveals chessboard structures comprising PbS and SnS modules with the number of atoms in the octahedral (M) sites counted as: $n1 = 18$ and $n2 = 8$ for tintinaite and $n1 = 30$ and $n2 = 16$ for izoklakeite. The homologue number can be calculated using the formula: $N = (n1/6)–1$ and $N = n2/4$ for PbS and SnS modules giving $N_{Tti} = 2$ and $N_{Iz} = 4$. A new $N = 3$ homologue, defined by $n = 12$ and $n = 24$ SnS and PbS modules, respectively, is identified as single or double units within areas with intergrowths between kobellite and izoklakeite. HAADF STEM imaging also reveals features attributable to lone electron pair micelles within the Sb-rich kobellite homologues. Atomic-resolution EDS STEM chemical mapping of Pb–Bi–Sb-sulfosalts shows a correlation with crystal structural modularity. The maps also highlight sites in the SnS modules of tintinaite in which $Sb > Bi$. Coherent nanoscale intergrowths between tintinaite and izoklakeite define jigsaw patterns evolving from chessboard structures and are considered to have formed during co-crystallisation of the two phases. Displacement textures and crosscutting veinlets (a few nm in width) are interpreted as evidence for superimposed syn-metamorphic deformation and are associated with the redistribution of Bi and Se. Imaging and mapping using HAADF STEM techniques is well suited to characterisation of Pb–Sb–Bi-sulfosalt phases, offering largely untapped potential to unravel the evolution of chessboard structures with applications across mineralogy but also extending into allied fields.

Keywords: HAADF STEM; nanoscale intergrowths; kobellite homologous series; tintinaite; izoklakeite; Boliden

(Received 10 December 2023; accepted 4 May 2024; Accepted Manuscript published online: 24 May 2024; Guest Editor: Qingze Chen)

Introduction

The kobellite homologous series is described by the formula $(Cu,Fe)_2M_{10N+6}S_{llN+13}$ for a 4 Å repeat where $M = Pb$, Bi and Sb; and N = homologue number (Makovicky and Mumme, 1986; Zakrzewski and Makovicky, 1986). Natural phases of the kobellite homologous series include kobellite and tintinaite with $N = 2$, and giessenite and izoklakeite with $N = 4$.

Tintinaite (Sb-rich) and kobellite (Bi-rich) are isostructural and form a continuous solid-solution pair with general formula: $(Cu_{2–x}Fe_x)[Pb_{10–2z+x}(Ag,Cu)_z(Sb_{1–y}Bi_y)_{16+z–x}]_{26}S_{35}$; $0 < x < 1$; $0 < y < 0.67$; $0 < z < 0.54$ (Moëlo *et al.*, 1995). Tintinaite from the type locality (TL) Tintina Mine, Yukon, Canada, was defined as the Sb-pure equivalent of kobellite from TL Vena, Sweden (Harris *et al.*, 1968; Moëlo *et al.*, 1984). The two species have space group *Pnnm* and cell parameters: $a = 22.30$ Å; $b = 34.00$ Å; and $c = 4.04$ Å for TL tintinaite (Harris *et al.*, 1986), and $a = 22.62$ Å; $b = 34.08$ Å; and $c = 4.04$ Å for TL kobellite (Nuffield, 1948).

Izoklakeite, ideally $[(Cu,Fe)_2Pb_{26.5}(Sb,Bi)_{19.5}S_{57}]$, is orthorhombic (space group *Pnnm*; $a = 34.07$ Å, $b = 37.98$ Å, and $c = 4.072$ Å, for specimen from Vena, Sweden; Zakrzewski and

Corresponding author: Cristiana L. Ciobanu; Email: cristiana.ciobanu@adelaide.edu.au
This paper is part of a thematic set on Nanominerals and mineral nanoparticles
Cite this article: Ciobanu C.L., Slattery A.D., Cook N.J., Wade B.P., Ehrig K., Wagner T. and Liu W. (2024) Kobellite homologues from the Boliden Au–Cu–(As) deposit, Sweden: jigsaw patterning via nanoscale intergrowths in chessboard structures. *Mineralogical Magazine* 1–21. https://doi.org/10.1180/mgm.2024.41

Makovicky, 1986) whereas its Bi-dominant analogue giessenite, ideally [$(Cu,Fe)_2$ $Pb_{26.4}(Bi,Sb)_{19.6}S_{57}$], is monoclinic (space group $P2_1/n$ $a = 34.34$ Å; $b = 38.05$ Å; $c = 4.06$ Å and $\beta = 90.33°$ for specimen from Bjorkåsen, Norway; Makovicky and Karup–Møller, 1986). Although no Sb-pure izoklakeite has been described, Bi-rich izoklakeite specimens with orthorhombic symmetry are documented from Lake Zervreila, Switzerland (Iz:Gie ratio 40:60; Armbruster and Hummel, 1987) and Gutaishan, China (Iz:Gie ratio 35:65; Li *et al.*, 2019). The general formula for a quasi-solid solution between izoklakeite and giessenite was given as: $(Cu_{2-x}Fe_x)[Pb_{26-2z+x}(Ag,Cu)_z(Sb_{1-y}Bi_y)_{20+z-x}]_{46}S_{57}$; $0 < x < 1$; $0.44 < y < 0.85$; $0 < z < 2.2$ (Moëlo *et al.*, 1995), even though the exact Sb:Bi ratio at which the symmetry changes is unknown (Moëlo *et al.*, 2008).

Distinguishing among these sulfosalt phases, and also compositionally similar but structurally unrelated phases such as jaskólskiite ($Cu_xPb_{2+x}(Sb,Bi)_{2-x}S_5$ ($x \approx 0.15$; Zakrzewski, 1984; Makovicky and Nørrestam, 1985), or jamesonite ($FePb_4Sb_6S_{14}$) (Niizeki and Buerger, 1957) can be difficult based solely on compositional data (e.g. electron probe microanalysis; EPMA). Unequivocal identification from EPMA data is impossible if the phases are intergrown at the sub-micrometre scale.

A prior study (Li *et al.*, 2019) demonstrated the utility of the high-angle annular dark field scanning transmission electron microscope (HAADF STEM) technique for visualising the crystal structures of coexisting kobellite and izoklakeite based on their characteristic modular structures. Here, we characterise intergrowths of Sb-rich kobellite homologues, modular minerals that extend down to the nanoscale and thus yield compositions at the scale of the microprobe beam that cannot be readily reconciled with one species or the other.

Boliden is a Palaeoproterozoic metamorphosed massive sulfide deposit in the Skellefte district of northern Sweden with characteristics interpreted as an ancient analogue to a modern high-sulfidation environment (Weihed *et al.*, 1996). The deposit was known for its high gold grades (average 15 ppm), massive arsenopyrite orebodies, and highly complex ore mineral assemblages (Grip and Wirstam, 1970; Wagner and Jonsson, 2001). An important part of the deposit is represented by sulfosalt-rich veins that host, alongside kobellite, a variety of other ore minerals including several Se-bearing sulfosalts (e.g. tetrahedrite, bournonite, boulangerite and meneghinite), Bi-selenides and -tellurides (tellurobismuthite, tetradymite and laitakarite), Hg-rich gold–silver alloys, gudmundite and native bismuth (Ödman, 1941; Grip and Wirstam, 1970; Wagner and Jonsson, 2001; Wagner *et al.*, 2007).

Selenium-rich kobellite has been reported previously from Boliden (Moëlo *et al.*, 1984 (reanalysis of a sample from Harris *et al.*, 1968); Wagner and Jonsson, 2001; Mumme *et al.*, 2013). Whereas the crystal structure of this Se-rich kobellite (Mumme *et al.*, 2013) differs only in minor ways from that determined for kobellite by Miehe (1971), the Sb concentration can vary in Boliden kobellite. A Sb/(Bi+Sb) ratio of ~0.5 is reported by Moëlo *et al.* (1984) and Mumme *et al.* (2013) and ~0.6 by Wagner and Jonsson (2001). On this basis, the Boliden kobellite reported by Wagner and Jonsson (2001) will hereafter be referred to as tintinaite.

This contribution describes co-existing Se-rich kobellite homologues (izoklakeite and tintinaite) that form micro- to nanoscale intergrowths in a specimen from the sulfosalt-rich veins at Boliden. By comparison with documented occurrences worldwide, we show these are among the most Sb-rich varieties that also contain Bi yet reported. We discuss the nature of the nanoscale intergrowths and show the presence of both primary and secondary textures. The primary intergrowths lead to formation of a new kobellite homologue during sulfosalt co-crystallisation, whereas the secondary textures record nanoscale remobilisation of Bi and Se during vein shearing. We aim to show how HAADF STEM imaging of modular structures is an appropriate tool to validate their building blocks and provide atomic-scale insights into formation of new phases as well as the primary versus secondary/overprinting origin of observed intergrowths.

Analytical methodology

The sample investigated (specimen 1061) originates from the Boliden Mineral AB collection (owned by Boliden AB, Sweden), that formed the basis of the first description of the deposit by Ödman (1941). The sample was collected from the 250 m level E in the mine, in room 28 ~213–216 metres away from the western part. Ore samples were mounted, polished and examined under reflected light and in back-scatter electron mode using an FEI Quanta 450 Field Emission Gun scanning electron microscope equipped with a silicon-drift energy-dispersive X-ray spectrometer (Adelaide Microscopy, The University of Adelaide).

Quantitative compositional data (spot analyses) and element-distribution maps were obtained using a Cameca SX-Five electron probe microanalyser in the same laboratory. The instrument runs *PeakSite v6.5* software for microscope operation and *Probe for EPMA* software for data acquisition and processing. The instrument is equipped with five tunable wavelength-dispersive spectrometers and was operated at 20 kV and 20 nA with a focussed beam. X-ray lines were as follows: S ($K\alpha$), Pb ($M\alpha$), Se ($L\alpha$), Te ($L\alpha$), Bi ($M\alpha$), As ($L\alpha$), Fe ($K\alpha$), Cu ($K\alpha$), Mn ($K\alpha$), Ag ($L\alpha$), Zn ($K\alpha$), Sb ($L\alpha$) and Cd($L\alpha$). All standards used were from P&H and Associates: galena for Pb and S; chalcopyrite for Cu and Fe; synthetic guanajuatite (Bi_2Se_3) for Bi and Se; gallium arsenide for As; galena for Pb; rhodonite for Mn; silver telluride for Ag; HgTe for Te; sphalerite for Zn; stibnite for Sb; and greenockite for Cd. Count times were 20 s on peak for all elements except Pb and S (15 s). Due to the complexity of off-peak interferences, traditional two point background analysis was initially acquired (20 s high and 20 s low), then through a function of the *Probe for EPMA* software these were turned into multipoint backgrounds utilising an exponential curve for background fitting. On-peak interferences were corrected using a range of standards in *Probe for EPMA*. Average minimum detection limits (99% C.I. in wt.%) were 0.008 for S; 0.05 for Pb and Ag; 0.04 for Bi and Cd; 0.03 for Se, Te, As, Cu and Zn; and 0.02 for Te, Sb, Fe and Mn. Qualitative X-ray mapping utilising the same instrument were acquired using Probe Image at settings of 20 kV and 200 nA at a pixel resolution of ~1 µm. Pixel dwell time was set to 2000 ms for enhanced sensitivity. Intensity maps were then coloured using *Surfer 10®* software distributed by Golden Software.

Additional element-distribution mapping was undertaken by laser ablation inductively coupled plasma mass spectrometry (LA–ICP–MS) using a RESOlution–LR 193 nm excimer laser attached to an Agilent 7900x Quadrupole ICP–MS. The following suite of isotopes were measured: ^{34}S, ^{57}Fe, ^{59}Co, ^{60}Ni, ^{65}Cu, ^{75}As, ^{77}Se, ^{107}Ag, ^{121}Sb, ^{125}Te, ^{197}Au, ^{206}Pb and ^{209}Bi. LA–ICP–MS trace-element distribution maps were generated by ablating sets of parallel line rasters in a grid across the sample surface. A square laser beam profile was used throughout with spot size varying between 11 and 16 μm to provide adequate spatial resolution for each map. Spacings between adjacent trenches and laser beam scan speed were modified to match spot size. Laser fluence was ~3.5 J/cm^2 using a repetition rate of 10 Hz. A 10 s background measurement was acquired before the ablation of each trench, followed by a 20 s delay after ablation. Two 74 μm-diameter spot analyses were made on STDGL3 and GSD-1G reference materials at 10 Hz before and after each map. All LA–ICP–MS trace-element distribution maps were processed with *Iolite* software.

Thinned <100 nm-thick foils for nanoscale investigation were prepared *in situ* from the surface of a polished mount attached to a copper grid using focused ion beam – scanning electron microscopy techniques. This was carried out on a FEI–Helios nanoLab dual focused ion beam and scanning electron microscope (FIB–SEM) at Adelaide Microscopy, The University of Adelaide. Extraction and thinning procedures followed Ciobanu *et al.* (2011).

HAADF STEM imaging and energy-dispersive spectroscopy (EDS) analysis reported here were performed using an ultra-high resolution, probe-corrected, FEI Titan Themis S/TEM in the same laboratory and previously used for imaging sulfosalts structures (e.g. Ciobanu *et al.* 2016; Li *et al.*, 2019). This instrument is equipped with a X-FEG Schottky source and Super-X EDS geometry. The Super-X EDS detector provides geometrically symmetric EDS detection with an effective solid angle of 0.8 sr. Probe correction delivered sub-Ångstrom spatial resolution and an inner collection angle greater than 50 mrad was used for HAADF imaging with a Fischione detector. Image acquisition, including a drift-corrected frame integration (DCFI) package and processing, was performed using both DigitalMicrograph^{TM} and Thermo-Scientific Velox software. Various filters were used to eliminate noise. EDS mapping was performed using Thermo-Scientific *Velox* software, which utilises standard Cliff–Lorimer quantification and included absorption correction optimised for both the Super-X detector geometry and also the effect of sample holder shadowing for the double-tilt Super-X holder used.

Diffraction indexing was performed using *Winwulff*© (JCrystalSoft) software. Data are stored in the American Mineralogist Crystal Structure Database (http://rruff.geo.arizona.edu/AMS/amcsd.php). Crystal structure models were generated in *CrystalMaker*® and image simulations using *STEM for xHREM*^{TM} (v4.1) software.

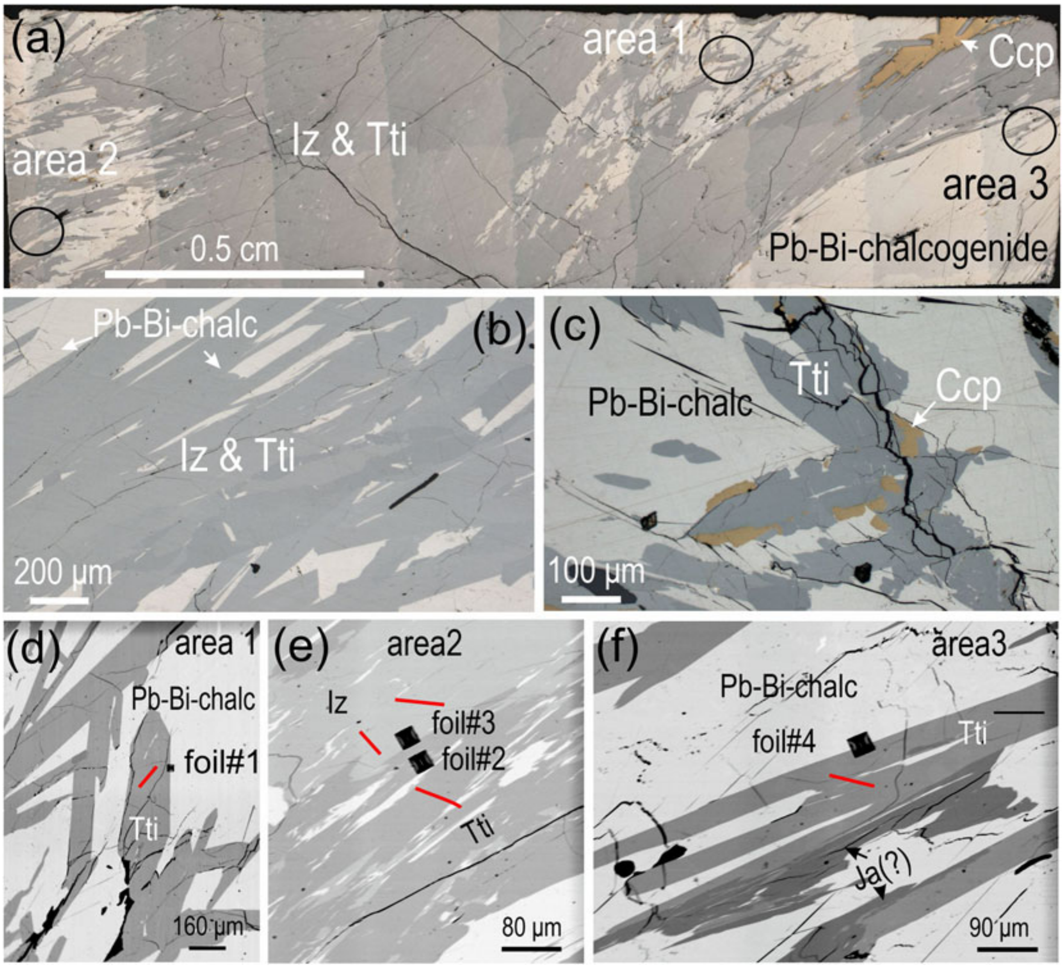

Figure 1. Reflected light microphotographs (a–c) and back-scattered electron (BSE) microscopy images (d–f) showing micrometre-scale intergrowths between tintinaite (Tti), izoklakeite (Iz) and Pb–Bi-chalcogenides (Pb-Bi-chalc) in sample/polished block 1061a. Note minor chalcopyrite (Ccp) is also present. Areas studied at the nanoscale are marked on the overall map of the sample (a). (d–f) Detailed images of areas 1–3 showing the stamps of FIB cuts from which the analysed S/TEM foils were prepared as well as the profiles for EPMA spot analyses (red lines). Tti–tintinaite.

Results

Specimen petrography – micrometre-scale characterisation

Both polished blocks analysed (1061 and 1061a) feature lamellar intergrowths between Pb–Sb–Bi-sulfosalts, identified as tintinaite and izoklakeite, and Bi–Pb chalcogenides which are readily distinguishable from the sulfosalts by their colour and brightness in reflected light (Fig. 1a–c). The bismuth minerals are associated with minor chalcopyrite, either interstitial within, or at the margins of the sulfosalts, and with pyrite, a major component of polished block 1061 (Supplementary Fig. S1). The three areas selected for nanoscale study (all in polished block 1061a) targeted contacts between acicular tintinaite lamellae and the Bi–Pb chalcogenide and the mutual contacts between the two sulfosalt species (Fig. 1d–f). Bi–Pb chalcogenide species are dominated by a new member of the aleksite series with the formula $PbBi_6(Te,Se)_6(S,Se)_4$ calculated from EPMA. The composition and crystal structure of this phase will be reported in detail elsewhere.

Trace-element distribution maps from LA–ICP–MS (polished block 1061) show that the sulfosalts concentrate minor Ag and Cd, whereas Se is a major component of the Bi-chalcogenide (Fig. 2a). A pyrite grain with a corroded margin at the mutual boundary with sulfosalts displays a Co-enriched rim but patchy distribution of As and Ni. Specks of relatively high Au concentration occur across the boundary between pyrite and the sulfosalt. Such textures are indicative of small-scale trace-element remobilisation during an overprinting event. This is also illustrated by the presence of laitakarite, $[(Bi_4(Se,S)_3]$, among other Bi-chalcogenide species from the tetradymite series, which occurs along trails crosscutting pre-existing phase boundaries (e.g. between sulfosalt

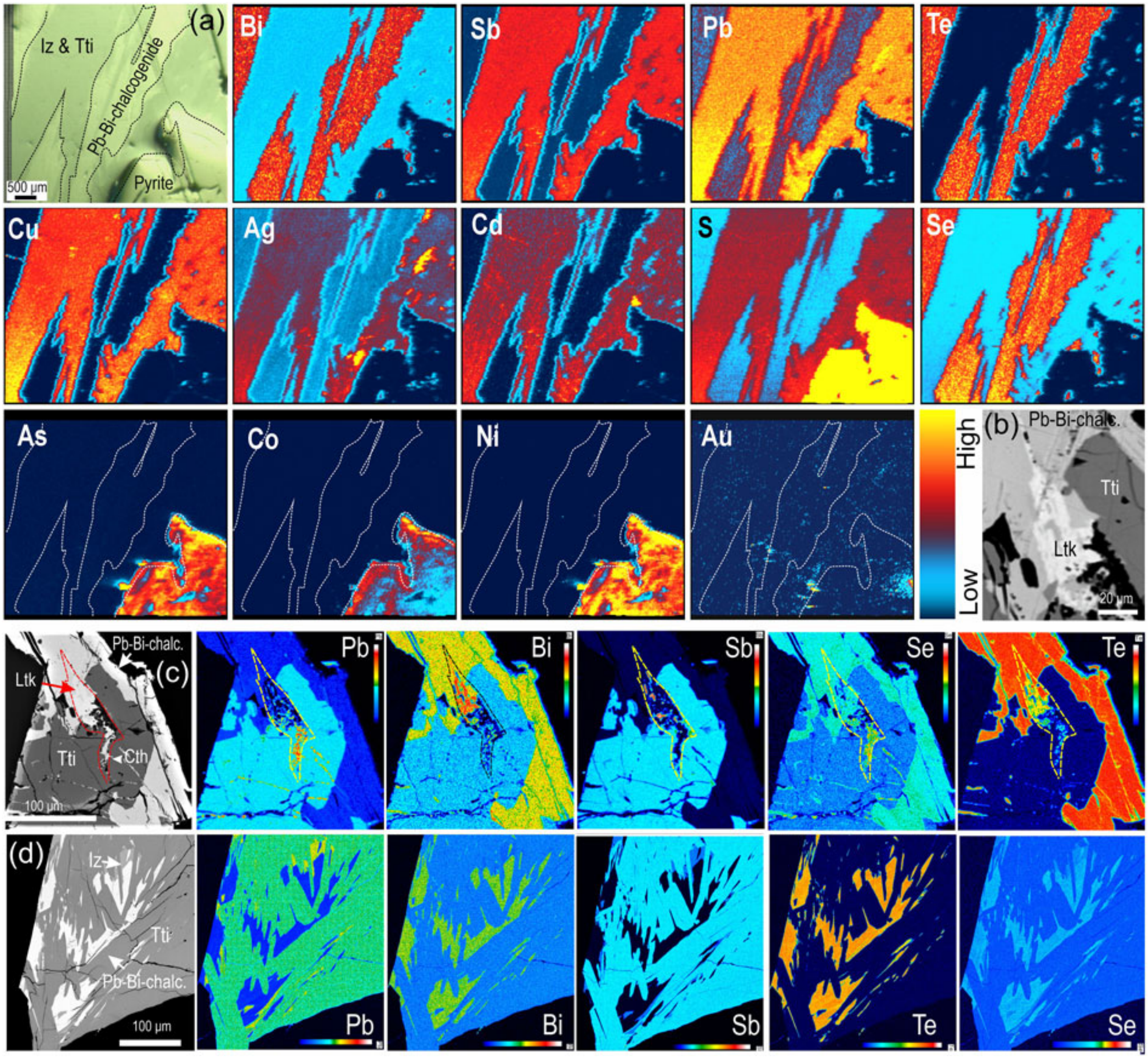

Figure 2. (a) LA–ICPMS element-distribution maps, (b) BSE image, and (c, d) EPMA element-distribution maps showing micrometre-scale distribution of main and minor/trace elements within intergrowths of tintinaite (Tti), izoklakeite (Iz) and Pb–Bi-chalcogenides (sample 1061). Note that Se is richest in the Pb–Bi-chalcogenide in (a, c, d). Silver is higher in the sulfosalt intergrowths whereas Au occurs as minute inclusions (high intensity spots) more abundant across a transect from pyrite into the Bi-mineral intergrowths in (a). (b) Inclusion of laitakarite (Ltk; Bi_4Se_3) at the junction between lamellae of Pb–Bi-chalcogenide and tintinaite. (c) Contact between tintinaite and Pb–Bi-chalcogenide is marked by fractures crosscutting the sulfosalt. These are shown by relative depletion in Pb, Bi and Sb and enrichment in Se. Such areas of element redistribution are accompanied by formation of laitakarite and clausthalite (Cth) marked by a red outline. (d) Tintinaite with interstitial Pb–Bi-chalcogenide. Note small area of izoklakeite (Iz) with the highest Pb concentration.

and aleksite series species, as seen on BSE images and EPMA maps; Fig. 2b, c). Fine-scale intergrowths between izoklakeite and tintinaite are readily seen on EPMA element-distribution maps for Pb (Fig. 2d).

Chemical composition

Compositional data for the two sulfosalts was obtained from both polished blocks. Mean compositions of izoklakeite and tintinaite are given in Tables 1, and 2–3, respectively. The complete EPMA datasets for kobellite homologues and associated (Bi, Se)-rich jamesonite are compiled as Supplementary Tables S1, S2 and S3. A selection of published data for kobellite homologues used for comparison are given in Supplementary Table S4.

To achieve an optimal correlation between micro- and nanoscale characterisation, EPMA of sample 1061a was carried out in areas immediately adjacent to the site of FIB cutting (Table 3). Analysis spots along short profiles are marked on Fig. 1d–f.

The ideal end-members of the two homologues as defined by Zakrzewski and Makovicky (1986) give a range of M^{2+}(Pb,Cd,Zn) relative to M^{3+}(Sb,Bi) ratios (cations with octahedral and prismatic coordination) correlated to the presence of atoms in tetrahedral coordination (T = Cu^+ and Fe^{2+}) by the formula:

$$N_{homologue} = x\frac{6M^{2+}+3M^{3+}}{4M^{3+}-M^{2+}} + (1-x)\frac{5M^{2+}+2M^{3+}}{4M^{3+}-M^{2+}}, \text{ where x} = \frac{T^{+}}{(T^{+}+T^{2+})} \text{ and } (1-x) = \frac{T^{2+}}{(T^{+}+T^{2+})}.$$

For the sake of simplicity, Ag^+ is included in the M^{2+} site and only Cu^+ is considered.

The M^{2+}:M^{3+} ratio is higher for $x = 0$ than for $x = 1$ (0.86 and 0.63 for kobellite–tintinaite, 1.56 and 1.3 for izoklakeite). The lowest ratio is obtained for $T = 0$, where $\frac{M^{2+}}{M^{3+}} = \frac{8N-8}{2N+14}$, i.e., 0.44 for $N = 2$ (kobellite or tintinaite) and 1.09 for $N = 4$ (izoklakeite). For N calculation we used the substitution: $Ag^+ + (Sb, Bi)^{3+} \rightarrow 2\ Pb^{2+}$, as considered for the formula calculation (Moëlo *et al.* 1995).

Izoklakeite has a mean composition $Iz_{60}Gie_{40}$ (Table 1) with the empirical formula: $(Cu_{1.88}Fe_{0.18})_{\Sigma 2.06}(Pb_{22.92}Ag_{1.47}Cd_{0.01}Zn_{0.01})_{\Sigma 24.41}(Sb_{13.12}Bi_{8.69})_{\Sigma 21.8}(S_{50.19}Se_{6.43}Te_{0.12})_{\Sigma 56.73}$. This corresponds to a Pb(Ag,Cd,Zn)-depleted, (Sb,Bi)-enriched composition relative to the ideal $N = 4$ homologue, $(Cu,Fe)_2Pb_{26}(Sb,Bi)_{20}S_{57}$, with substitution factor $x = 1$ (Zakrzewski and Makovicky, 1986). The mean homologue number N is 3.83 using calculations based on 105 atoms per formula unit (apfu) (Table 4).

Table 1. Electron probe compositional data for izoklakeite.

	All (*n* = 21)				Sample 1061 (*n* = 8)				Sample 1061a (area 2) (*n* = 13)			
	Mean*	S.D.	Min	Max	Mean	S.D.	Min	Max	Mean	S.D.	Min	Max
Wt.%												
Pb	45.08	0.35	44.35	45.58	44.73	0.20	44.35	45.04	45.30	0.23	44.93	45.58
Sb	15.16	0.25	14.52	15.49	14.97	0.30	14.52	15.27	15.28	0.11	15.05	15.49
Bi	17.24	0.28	16.69	17.95	17.40	0.29	16.95	17.95	17.13	0.22	16.69	17.49
Cu	1.13	0.03	1.08	1.18	1.12	0.02	1.08	1.15	1.14	0.03	1.09	1.18
Ag	1.50	0.10	1.32	1.72	1.46	0.11	1.32	1.60	1.53	0.09	1.42	1.72
Fe	0.09	0.01	0.07	0.11	0.09	0.01	0.07	0.10	0.10	0.01	0.08	0.11
Zn	0.01	0.01	<mdl	0.05	0.01	0.01	<mdl	0.02	0.01	0.01	<mdl	0.05
Cd	0.01	0.03	<mdl	0.09	0.02	0.03	<mdl	0.07	0.01	0.03	<mdl	0.09
S	15.27	0.12	15.06	15.49	15.17	0.08	15.06	15.32	15.34	0.09	15.21	15.49
Se	4.82	0.21	4.55	5.29	5.05	0.15	4.91	5.29	4.67	0.07	4.55	4.79
Te	0.14	0.06	0.08	0.27	0.22	0.03	0.16	0.27	0.10	0.01	0.08	0.13
Total	100.3	0.38	99.5	100.9	100.2	0.21	100.0	100.6	100.4	0.46	99.5	100.9
Formulae calculated on the basis of 105 apfu												
Pb	22.92	0.14	22.60	22.94	22.80	0.11	22.60	22.94	22.99	0.10	22.85	23.14
Sb	13.12	0.19	12.58	13.25	12.99	0.24	12.58	13.25	13.20	0.07	13.08	13.30
Bi	8.69	0.14	8.46	9.10	8.80	0.16	8.57	9.10	8.62	0.08	8.46	8.74
Ag	1.47	0.10	1.30	1.56	1.43	0.10	1.30	1.56	1.49	0.09	1.39	1.69
Cu	1.88	0.04	1.80	1.92	1.86	0.04	1.80	1.92	1.89	0.04	1.81	1.95
Fe	0.18	0.02	0.13	0.19	0.16	0.02	0.13	0.19	0.18	0.02	0.15	0.21
Zn	0.01	0.02	0.00	0.04	0.01	0.02	0.00	0.04	0.01	0.02	0.00	0.07
Cd	0.01	0.03	0.00	0.06	0.02	0.03	0.00	0.06	0.01	0.03	0.00	0.08
S	50.19	0.23	49.74	50.43	49.99	0.23	49.74	50.43	50.30	0.12	50.10	50.49
Se	6.43	0.30	6.06	7.10	6.76	0.20	6.56	7.10	6.22	0.10	6.06	6.37
Te	0.12	0.05	0.07	0.23	0.18	0.03	0.13	0.23	0.08	0.01	0.07	0.10
Ev (%)	1.35	0.66	−0.42	1.23	0.69	0.54	−0.42	1.23	1.75	0.31	1.07	2.03
End-member proportions												
% Iz Sb/(Bi+Sb)	60	0.70	58.2	60.7	60	0.85	58.2	60.7	60	0.28	59.9	61.0
% Gie Bi/(Bi+Sb)	40	0.70	39.0	41.8	40	0.85	39.3	41.8	40	0.28	39.0	40.1
Cu+Fe	2.06	0.05	1.94	2.08	2.00	0.05	1.90	2.08	2.10	0.05	2.00	2.14
Pb+2*Ag+Cd+Zn	25.88	0.20	25.57	25.93	25.7	0.14	25.6	25.93	26.0	0.14	25.8	26.29
Bi+Sb–Ag	20.34	0.11	20.14	20.45	20.3	0.09	20.2	20.45	20.3	0.12	20.1	20.52
Total *M*	48.27	0.19	47.81	48.25	48.1	0.15	47.8	48.25	48.4	0.08	48.2	48.50
S+Se+Te	56.73	0.19	56.50	57.19	56.90	0.15	56.80	57.19	56.6	0.08	56.50	56.78
N homologue	3.83	0.05	3.76	3.85	3.80	0.03	3.80	3.85	3.85	0.05	3.80	3.94

*Weighted mean. Mdl –method detection limit; S.D. – standard deviation

Table 2. Electron probe compositional data for tintinaite.

	All (*n* = 47)				sample 1061 (*n* = 15)				sample 1061a (areas 1–3) (*n* = 32)			
	Mean	S.D.	Min	Max	Mean	S.D.	Min	Max	Mean	S.D.	Min	Max
Wt.%												
Pb	37.18	0.70	36.07	38.36	36.43	0.28	36.07	36.87	37.53	0.53	36.58	38.36
Sb	21.06	0.82	19.89	22.42	20.43	0.54	19.89	21.39	21.36	0.77	20.29	22.42
Bi	18.54	1.29	16.61	20.53	19.38	0.94	17.96	20.53	18.14	1.26	16.61	20.03
Cu	1.41	0.06	1.30	1.54	1.43	0.03	1.38	1.49	1.40	0.06	1.30	1.54
Ag	0.32	0.05	0.21	0.44	0.34	0.02	0.31	0.39	0.31	0.05	0.21	0.44
Fe	0.70	0.05	0.61	0.79	0.66	0.03	0.61	0.74	0.72	0.05	0.63	0.79
Zn	0.02	0.02	<mdl	0.06	0.03	0.01	<mdl	0.05	0.02	0.02	<mdl	0.06
Cd	0.10	0.09	0.00	0.38	0.10	0.03	0.04	0.16	0.11	0.11	0.00	0.38
S	17.52	0.16	17.19	17.82	17.34	0.10	17.19	17.56	17.61	0.10	17.46	17.82
Se	3.30	0.11	3.03	3.53	3.37	0.15	3.03	3.53	3.27	0.06	3.13	3.36
Te	0.01	0.02	<mdl	0.12	0.01	0.01	<mdl	0.04	0.01	0.02	<mdl	0.12
Total	100.2	0.61	98.7	101.2	99.5	0.36	98.74	99.96	100.5	0.44	99.5	101.2
Formulae calculated on the basis of 63 apfu												
Pb	10.58	0.12	10.38	10.80	10.46	0.07	10.38	10.59	10.63	0.10	10.45	10.80
Sb	10.20	0.33	9.73	10.69	9.99	0.25	9.73	10.36	10.30	0.32	9.82	10.69
Bi	5.23	0.40	4.63	5.85	5.52	0.27	5.12	5.85	5.10	0.38	4.63	5.65
Ag	0.18	0.03	0.11	0.24	0.19	0.01	0.17	0.21	0.17	0.03	0.11	0.24
Cu	1.31	0.06	1.20	1.43	1.34	0.03	1.29	1.40	1.29	0.06	1.20	1.43
Fe	0.74	0.05	0.65	0.82	0.70	0.03	0.65	0.79	0.76	0.05	0.66	0.82
Zn	0.02	0.02	0.00	0.05	0.02	0.01	0.00	0.04	0.02	0.02	0.00	0.05
Cd	0.05	0.05	0.00	0.20	0.05	0.02	0.02	0.08	0.06	0.06	0.00	0.20
S	32.22	0.09	31.99	32.43	32.18	0.12	31.99	32.43	32.25	0.06	32.15	32.37
Se	2.46	0.09	2.28	2.67	2.54	0.11	2.28	2.67	2.43	0.04	2.34	2.49
Te	0.00	0.01	0.00	0.05	0.00	0.01	0.00	0.02	0.00	0.01	0.00	0.05
Ev (%)	1.69	0.39	0.35	2.14	1.55	0.49	0.35	2.01	1.75	0.31	0.93	2.14
End-member proportions												
%Tti Sb/(Bi+Sb)	66	2.43	62.6	69.6	64	1.69	62.6	66.9	67	2.33	63.6	69.6
%Kbl Bi/(Bi+Sb)	34	2.43	30.4	37.4	36	1.69	33.1	37.4	33	2.33	30.4	36.4
Cu+Fe	2.05	0.03	1.97	2.13	2.0	0.02	2.01	2.09	2.05	0.04	1.97	2.13
Pb+2*Ag+Cd+Zn	11.01	0.12	10.81	11.22	10.9	0.07	10.81	11.04	11.05	0.11	10.85	11.22
Bi+Sb–Ag	15.26	0.08	15.12	15.47	15.3	0.08	15.16	15.47	15.23	0.07	15.12	15.41
Total *M*	28.31	0.06	28.11	28.38	28.3	0.07	28.11	28.36	28.32	0.05	28.21	28.38
S+Se+Te	34.69	0.06	34.62	34.89	34.7	0.07	34.64	34.89	34.68	0.05	34.62	34.79
N homologue	2.05	0.02	2.00	2.08	2.03	0.02	2.00	2.06	2.05	0.02	2.01	2.08

Mdl –method detection limit; S.D. – standard deviation

The mean tintinaite composition is $Tti_{66}Kbl_{34}$ with the empirical formula: $(Cu_{1.31}Fe_{0.74})_{\Sigma 2.05}(Pb_{10.58}Ag_{0.18}Cd_{0.05}Zn_{0.02})_{\Sigma 10.83}(Sb_{10.2}Bi_{5.23})_{\Sigma 15.43}(S_{32.22}Se_{2.46})_{\Sigma 34.7}$ and calculated $N = 2.05$ (Tables 2 and 4). Tintinaite is richer in Pb(Ag,Cd,Zn) and slightly poorer in (Sb,Bi) than the ideal $N = 2$ homologue, $(Cu,Fe)_2Pb_{10}(Sb,Bi)_{16}S_{35}$, with substitution factor $x = 1$ (Zakrzewski and Makovicky, 1986), thus opposite to the trend shown by izoklakeite.

The Sb-rich sulfosalt occurring as the darkest lamellae on BSE images from FB area 3 (Fig. 1f) contains Fe and was identified as jamesonite $(Fe_{0.99}Cu_{0.01})_{1.00}(Pb_{3.89}Cd_{0.03})_{3.91}(Sb_{5.14}Bi_{1.03})_{6.17}(S_{13.14}Se_{0.78})_{13.92}$ (Supplementary Table S4). Notably, Se is present in this third sulfosalt, albeit at a lower concentration (2.81 wt.%) than in izoklakeite (4.82 wt.%) or tintinaite (3.3 wt.%).

There are, however, subtle compositional variations within each sulfosalt from the two polished blocks and, for tintinaite, also between the three analysed areas (Fig. 3; Tables 1–3; Supplementary Tables S1 and S2). Both izoklakeite and tintinaite show a slight relative depletion in Pb (Ag,Cd,Zn) in the pyrite-rich sample (1061) compared to the sulfide-poor sample (1061a). Tintinaite coexisting with izoklakeite (area 2, 1061a) is lowest in Pb(Ag,Cd,Zn), whereas tintinaite coexisting with (Bi, Se)-rich jamesonite is lowest in Sb+Bi but highest in Pb(Ag,Cd, Zn) (Fig. 3). Izoklakeite displays a more marked Pb(Ag,Cd,Zn) variation between the two samples than tintinaite.

Nanoscale characterisation

Three areas of the Boliden specimen were investigated in four S/TEM foils obtained from polished block 1061a as marked on Fig. 1a: one (foil #1) from area 1, two (foils #2 and #3) from area 2, and one (foil #4) from area 3 (Fig. 4a–d). Contacts between tintinaite and the Pb–Bi-chalcogenide are sharp (Fig. 4a,b), with a thin sliver of Sb-rich Bi sulfosalt, a few µm wide observed in foil #1 which is obtained from the area where no µm-scale lamellae of tintinaite are identified. Foils obtained across the contacts between tintinaite and izoklakeite (Fig. 4c,d) display intergrowths between the two phases, and feature µm- to sub-µm-scale patches of the Pb–Bi-chalcogenide. EDS STEM maps across the three phases in foil #1 show a relative enrichment of Ag in tintinaite and the Pb–Bi-chalcogenide, whereas the Sb-rich Bi-sulfosalt is also enriched in Fe (Fig. 4e), consistent with jamesonite. Selenium is concentrated within the Pb–Bi-chalcogenide.

Nanoscale intergrowths between tintinaite and izoklakeite are widespread along the direct contacts between the two phases (Fig. 5). Typically, the intergrowths consist of lamellae of one species within the other forming rhythmic banding within fine-grained aggregates (Fig. 5a–c). The banding is however irregular, with rhythms that change across the same grain, and with lamellae thickness that varies from a few nm to several tens of nm in width. The Pb–Bi-chlacogenide is embayed into the sulfosalt

Table 3. Electron probe compositional data for tintinaite in three areas of sample 1061a, highlighting local variation.

	area2				area 1				area 3			
	n = 9	S.D.	Min.	Max.	*n* = 8	S.D.	Min.	Max.	*n* = 15	S.D.	Min.	Max.
Wt.%												
Pb	36.92	0.26	36.58	37.30	37.42	0.30	37.05	37.86	37.96	0.31	37.41	38.36
Sb	20.40	0.07	20.29	20.51	21.02	0.21	20.72	21.30	22.12	0.12	21.95	22.42
Bi	19.78	0.25	19.30	20.03	18.57	0.30	18.19	18.99	16.93	0.19	16.61	17.29
Cu	1.48	0.03	1.45	1.54	1.38	0.02	1.36	1.42	1.355	0.03	1.30	1.40
Ag	0.34	0.05	0.28	0.44	0.32	0.04	0.26	0.37	0.284	0.04	0.21	0.34
Fe	0.66	0.02	0.63	0.68	0.75	0.02	0.71	0.77	0.748	0.02	0.71	0.79
Zn	0.03	0.02	<mdl	0.06	0.01	0.02	<mdl	0.04	0.024	0.02	<mdl	0.05
Cd	0.06	0.05	<mdl	0.10	0.03	0.04	<mdl	0.10	0.180	0.12	<mdl	0.38
S	17.55	0.07	17.47	17.66	17.54	0.06	17.46	17.64	17.69	0.07	17.55	17.82
Se	3.21	0.04	3.16	3.26	3.27	0.06	3.13	3.31	3.30	0.05	3.20	3.36
Te	<mdl		<mdl	<mdl	<mdl		<mdl	<mdl	0.011	0.03	<mdl	0.12
Total	100.4	0.53	99.5	101.0	100.3	0.32	100.0	100.8	100.6	0.42	99.8	101.2
Calculated formulae on the basis of 63 apfu												
Pb	10.51	0.04	10.45	10.59	10.64	0.07	10.57	10.76	10.70	0.06	10.59	10.80
Sb	9.88	0.04	9.82	9.96	10.17	0.10	10.02	10.30	10.61	0.04	10.51	10.69
Bi	5.58	0.06	5.48	5.65	5.24	0.09	5.12	5.36	4.73	0.06	4.63	4.83
Ag	0.19	0.03	0.15	0.24	0.17	0.02	0.14	0.20	0.15	0.02	0.11	0.19
Cu	1.38	0.03	1.34	1.43	1.28	0.02	1.26	1.32	1.24	0.03	1.20	1.29
Fe	0.70	0.02	0.66	0.72	0.79	0.02	0.75	0.82	0.78	0.02	0.75	0.82
Zn	0.03	0.02	0.00	0.05	0.01	0.02	0.00	0.04	0.02	0.02	0.00	0.05
Cd	0.03	0.02	0.00	0.05	0.02	0.02	0.00	0.05	0.09	0.06	0.00	0.20
S	32.30	0.07	32.18	32.37	32.24	0.06	32.17	32.32	32.22	0.04	32.15	32.30
Se	2.40	0.03	2.36	2.44	2.44	0.04	2.34	2.47	2.44	0.03	2.37	2.49
Te	0.00	0.00	0.00	0.00	0.00	0.00	0.00	0.00	0.00	0.01	0.00	0.05
Ev (%)	1.58	0.47	0.93	2.02	1.73	0.30	1.32	2.14	1.85	0.13	1.53	2.01
End-member proportions												
%Tti [Sb/(Bi+Sb)]	64	0.30	63.6	64.4	66	0.58	65.2	66.8	69	0.29	68.6	69.6
%Kbl [Bi/(Bi+Sb)]	36	0.30	35.6	36.4	34	0.58	33.2	34.8	31	0.29	30.4	31.4
Cu+Fe	2.10	0.03	2.05	2.13	2.10	0.02	2.03	2.11	2.00	0.03	1.97	2.09
Pb+2* [Ag+Cd+Zn]	10.9	0.09	10.85	11.11	11.0	0.06	10.94	11.10	11.1	0.09	10.95	11.22
Bi+Sb–Ag	15.3	0.06	15.22	15.41	15.2	0.04	15.17	15.29	15.2	0.06	15.12	15.31
Total *M*	28.3	0.07	28.21	28.38	28.3	0.05	28.25	28.38	28.3	0.03	28.25	28.38
S+Se+Te	34.7	0.07	34.62	34.79	34.7	0.05	34.62	34.75	34.7	0.03	34.62	34.75
N homologue	2.05	0.02	2.01	2.08	2.04	0.01	2.03	2.06	2.06	0.02	2.01	2.08

Mdl – method detection limit; S.D. – standard deviation

aggregates (Fig. 5b). Sharp changes in banding patterns are observed across grain contacts (Fig. 5c). EDS STEM maps of sulfosalt intergrowths show significant compositional changes in some elements, particularly Sb > Pb or S > Se in tintinaite versus izoklakeite, whereas the variation in Bi is more subtle (Fig. 5d,e). Izoklakeite is richer in minor Ag but poorer in Fe relative to tintinaite. Clusters of Bi–Se nanoparticles (NPs) decorate the margins of tintinaite lamellae which are either truncated or displaced by fractures (Fig. 5e).

Chemical structural modularity: the main building modules in tintinaite and izoklakeite

PbS and SnS modules are readily identified on the [001] zone axis of tintinaite and izoklakeite (Fig. 6a–d). These are recognised on HAADF STEM images as blocks with the number of heavy atoms *M* (bright dots on images) counted as: $n1 = 18$ and $n2 = 8$ for tintinaite, and $n1 = 30$ and $n2 = 16$ for izoklakeite (overlays on Fig. 6a,c). Using the formulae $M_{6(N+1)}S_{7N+9}$ and $M_{4N}S_{4(N+1)}$ (M = Bi, Sb and Pb) (Makovicky and Mumme, 1986; Zakrzewski and Makovicky, 1986), we can calculate the homologue number N from the M sites as: $N = n1/6 - 1$ and $N = n2/4$ for PbS and SnS modules giving $N_{Kbl} = 2$ and $N_{Iz} = 4$. The atomic arrangements for the larger SnS modules are shown as given by Li *et al.* (2019) and Makovicky and Mumme (1986).

The crystal structure models show a very good correlation with the STEM simulations and atomic-scale images for the two sulfosalts (Fig. 7). The structures (Miehe, 1971; Makovicky and Mumme, 1986) consist of PbS and SnS modules (referred to as rods in earlier descriptions of Makovicky and Mumme, 1986; Zakrzewski and Makovicky, 1986) that alternate on both *a* and *b* directions (highlighted by overlays on crystal models, STEM simulations and images in Fig. 7). Tetrahedral-coordinated cations (T = Cu and Fe) are nested at the module interfaces. The HAADF STEM images show patterns of dark lines, particularly visible through the centre of the SnS modules in izoklakeite. These correspond to weaker/longer Sb(Bi)–S bonds between adjacent polyhedra.

High-resolution EDS STEM element distribution maps and their overlays show a good match with atom-fill models for the two sulfosalts (Figs 8, 9, and Supplementary Figs S2 and S3). Overlays of Sb–Pb–Bi–Fe distribution maps and a crystal model for tintinaite show an excellent correlation with the two building modules (Fig. 8a). The distribution of Fe in the tetrahedral sites flanking the corners of the SnS module and in the kinks of the PbS module are very well depicted for tintinaite. Overlays of Sb–Pb–Bi distribution maps with the HAADF STEM image

Table 4. Calculated *N* values[1] for sulfosalts in this study compared with literature data.

Sample label	Calc. on 63 apfu	Ratio Tti:Kbl	Reference	Locality details
Tintinaite–kobellite	N_H (= 2)			
Tintina	2.17	100:0	Moëlo *et al.* (1984)	Tintina Mine, Yukon, Canada
Boliden	2.05	67:33	1061a (this study)	Boliden, Sweden
	2.03	64:36	1061 (this study)	
Boliden 3	2.09	59:41	Wagner and Jonsson (2001)	Boliden, Sweden
Boliden 2	1.95	52:48	Mumme *et al.* (2013)	Boliden, Sweden
Boliden1	2.15	50:50	Moëlo *et al.* (1984)	Boliden, Sweden
Pedra Luz2	2.14	65:35	Moëlo *et al.* (1995)	Pedra Luz, Portugal
Uhorna	1.96	60:40	Pršek and Peterec (2008)	Úhorná, Spišsko Gemerské Rudohorie Mts., Slovakia
Rossland	1.96	56:44	Moëlo *et al.* (1995)	Rossland, British Columbia, Canada
Korunka Mine	2.32	44:56	Miehe (1971)	Korunka Mine, Gelnica, Slovakia
Pedra Luz1	1.92	40:60	Moëlo *et al.* (1995)	Pedra Luz, Portugal
Gutaishan	2.02	39:61	Li *et al.* (2019)	Gutaishan, China
Hvena	2.18	37:63	Moëlo *et al.* (1984)	Vena, Sweden
Les Chalanches	2.25 2.61* 2.09**	34:66	Moëlo *et al.* (1995)	Les Chalanches, Grenoble, France
Raleigh	2.25 2.37* 2.12**	34:66	Moëlo *et al.* (1984)	Raleigh, USA

Sample label	Calc. on 105 apfu	Ratio Iz:Gie	Reference	Locality details
Izoklakeite	N_H (= 4)			
Boliden	3.80	60:40	Bol 1061 (this study)	Boliden, Sweden
	3.85		Bol 1061a (this study)	
Izok Lake	4.17	53:47	Harris *et al.* (1986)	Izok Lake, Northwest Territories, Canada
Bazoges1	4.01	53:47	Moëlo *et al.* (1995)	Bazoges, France
Vena	4.14	51:49	Zakrzewski and Makovicky (1986)	Vena, Sweden
Les Chalanches	3.73 4.01* 3.82**	42:58	Moëlo *et al.* (1995)	Les Chalanches, Grenoble, France
Lake Zervreila	4.54 4.08***	40:60	Armbruster and Hummel (1987)	Lake Zervreila, Vals, Switzerland
Bazoges2	4.09	36:64	Moëlo *et al.* (1995)	Bazoges, France
Gutaishan	4.12	35:65	Li *et al.* (2019)	Gutaishan, China
Giessenite	N_H (= 4)			
Binntal	3.98	19.5:80.5	Graeser and Harris (1986)	Giessen, Binn, Switzerland
Bjorkåsen	4.19	15:85	Makovicky and Karup-Møller (1986)	Bjorkåsen, Norway

[1] Calculations used the formula for the tintinaite–kobellite and izoklakeite–giessenite series given by Moëlo *et al.* (1995): tintinaite–kobellite: $(Cu_{2-x}Fe_x)[Pb_{10-2z+x}(Ag,Cu)_z(Sb_{1-y}Bi_y)_{16+z-x}]_{\Sigma 26}S_{35}$, with $0 \leq x \leq 1$; $0 \leq y \leq 0.67$; $0 \leq z \leq 0.54$, and izoklakeite–giessenite: $(Cu_{2-x}Fe_x)[Pb_{26-2z+x}(Ag,Cu)_z(Sb_{1-y}Bi_y)_{20+z-x}]_{\Sigma 46}S_{57}$, with $0 \leq x \leq 1$; $0.44 \leq y \leq 0.85$; $0 \leq z \leq 2.2$, with addition of the following as indicated: * excess Cu on Pb; ** excess Cu on (Sb+Bi); ***Ag incorporated on (Sb,Bi) sites.

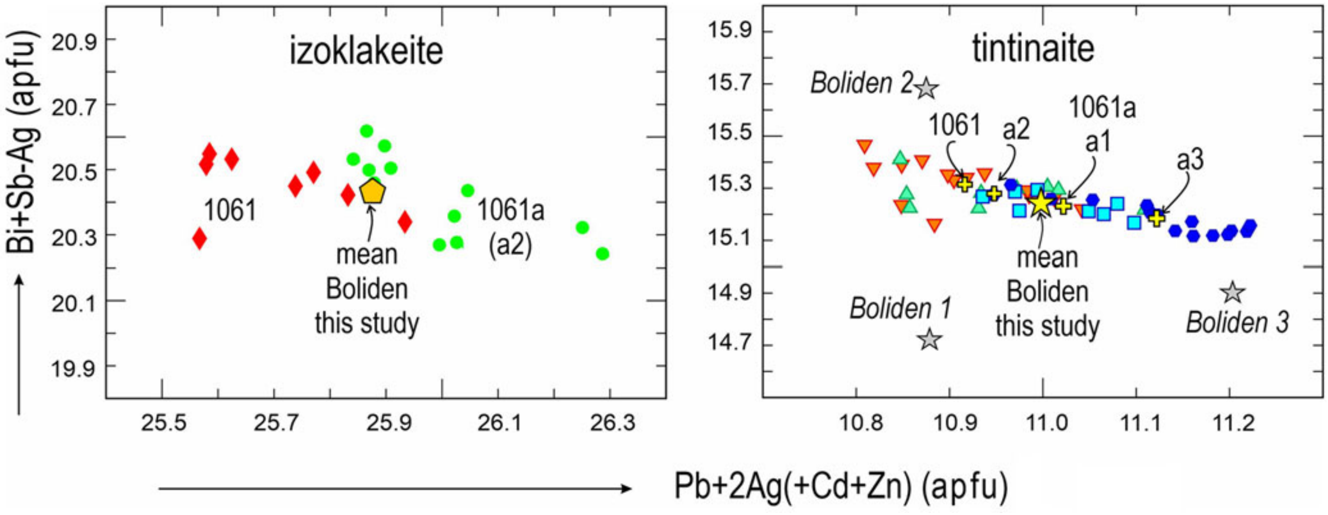

Figure 3. Binary plots of Bi+Sb–Ag vs. Pb+2Ag+Cd+Zn (apfu) showing subtle differences in chemistry of izoklakeite and tintinaite between the two analysed samples (as labelled). Data from Tables 1–3 and Supplementary Tables S1–3. For comparison, data for kobellite–tintinaite from Moëlo *et al.* (1984), Mumme *et al.* (2013) and Wagner and Jonsson (2001) are plotted and labelled as *Bol1*, *Bol2* and *Bol3*, respectively.

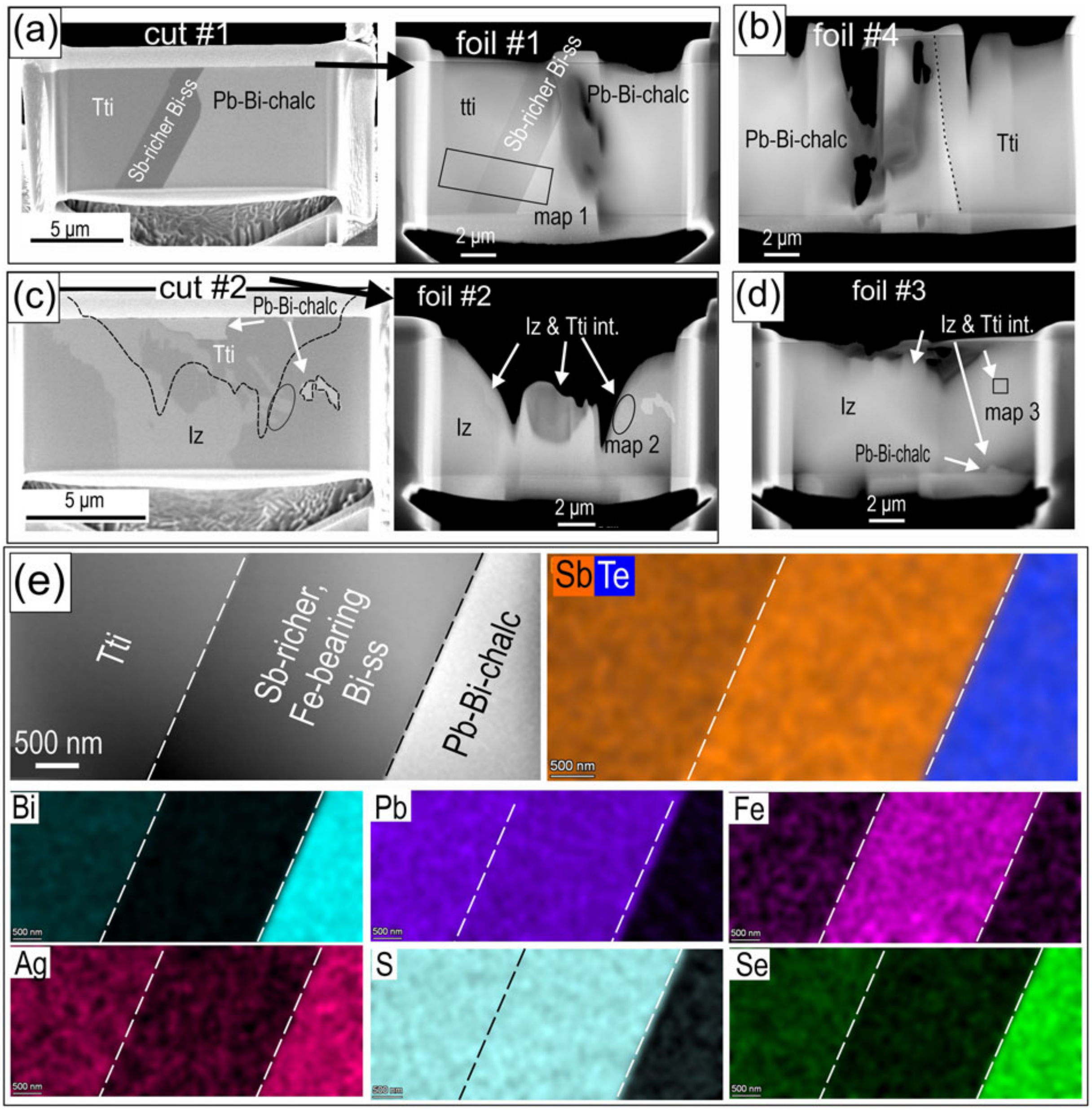

Figure 4. (a–d) Images showing the four foils as labelled (from polished block 1061a, details in text) which have targeted contacts between the three components in the lamellar intergrowths, tintinaite (Tti), izoklakeite (Iz) and Pb–Bi-chalcogenide. Foils #1 and #2 are shown both before (left) and after (right) thinning. (e) HAADF STEM image and EDS STEM element-distribution maps of the grain boundary between tintinaite and Pb–Bi-chalcogenide (marked by rectangle 'map 1' in (a)) showing the presence of an Sb-rich bismuth sulfosalt lamella between the two phases. Note the relative depletion in Bi, Ag and Se, and the marked Fe enrichment of this lamella relative to tintinaite. The contacts between tintinaite and izoklakeite in foils #3 and #4 are marked by the presence of small Pb–Bi-chalcogenide inclusions.

also reproduce the two modules, albeit with less accuracy than for tintinaite (Fig. 8b). Nonetheless, the distribution of SnS modules is well resolved for izoklakeite.

In closer detail, the EDS STEM element-distribution maps for Pb, Sb, Bi and Fe in tintinaite show the distribution of these elements throughout the structure whereby four Bi/Sb sites are at centre of the SnS modules; these are surrounded by Pb atoms (Fig. 9a). Taking the crystal model for the asymmetric unit cell from Miehe (1971), there are seven Bi/Sb sites of which two have 0.5:0.5 ratios, whereas the others, except site #1 where Sb is twice as much as Bi (0.33:0.67), have occupancies in which Bi > Sb (Fig. 9b). The map for Sb suggests, however, that occupancy is Sb > Bi for sites #3, 4 and 5 (Fig. 9a). This agrees with the higher tintinaite component in the Boliden $N = 2$ kobellite homologue compared with the specimen studied by Miehe (1971) – 66 mol.% and 44 mol.% tintinaite, respectively.

Nanoscale intergrowths and defects in tintinaite–izoklakeite

Considering that $b_{\mathrm{Kbl\sim Tti}}$ and a_{Iz} are equal (~34 Å), coherent syntactic intergrowths along these directions are commonly formed (Fig. 10a–c). In some cases, however, the boundaries between such intergrowths show stepwise displacements with small-scale re-shaping and are accompanied by a protrusion of Bi-rich stringers (Fig. 10a). Likewise, the boundaries between grains featuring rhythmic intergrowths of variable width are curvilinear, with small

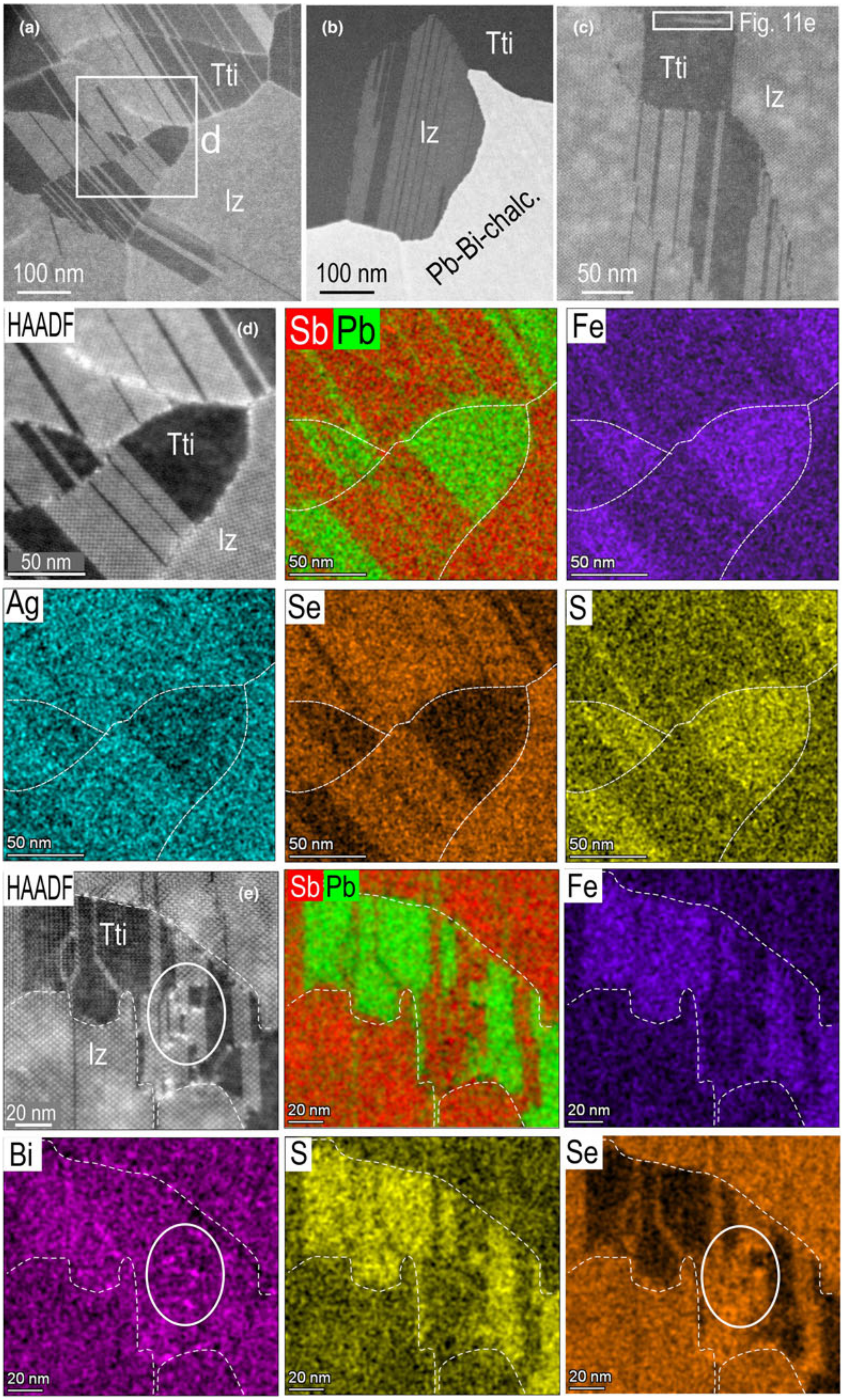

Figure 5. Intergrowths between tintinaite (Tti), izoklakeite (Iz) and Pb–Bi-chalcogenide as HAADF STEM images (a–c) and EDS STEM maps 2 and 3 (d, e) marked on Fig. 4c and d. The mapped areas are marked by the rectangles as labelled. Note that contacts display smaller grains with fine, nanometre-scale lamellar intergrowths between the two sulfosalts. (d) (e) Maps showing the relative increase in Pb, Fe and S and decrease in Se between tintinaite and izoklakeite. Remobilisation of Se (circled area) along the contacts between the finest intergrowths.

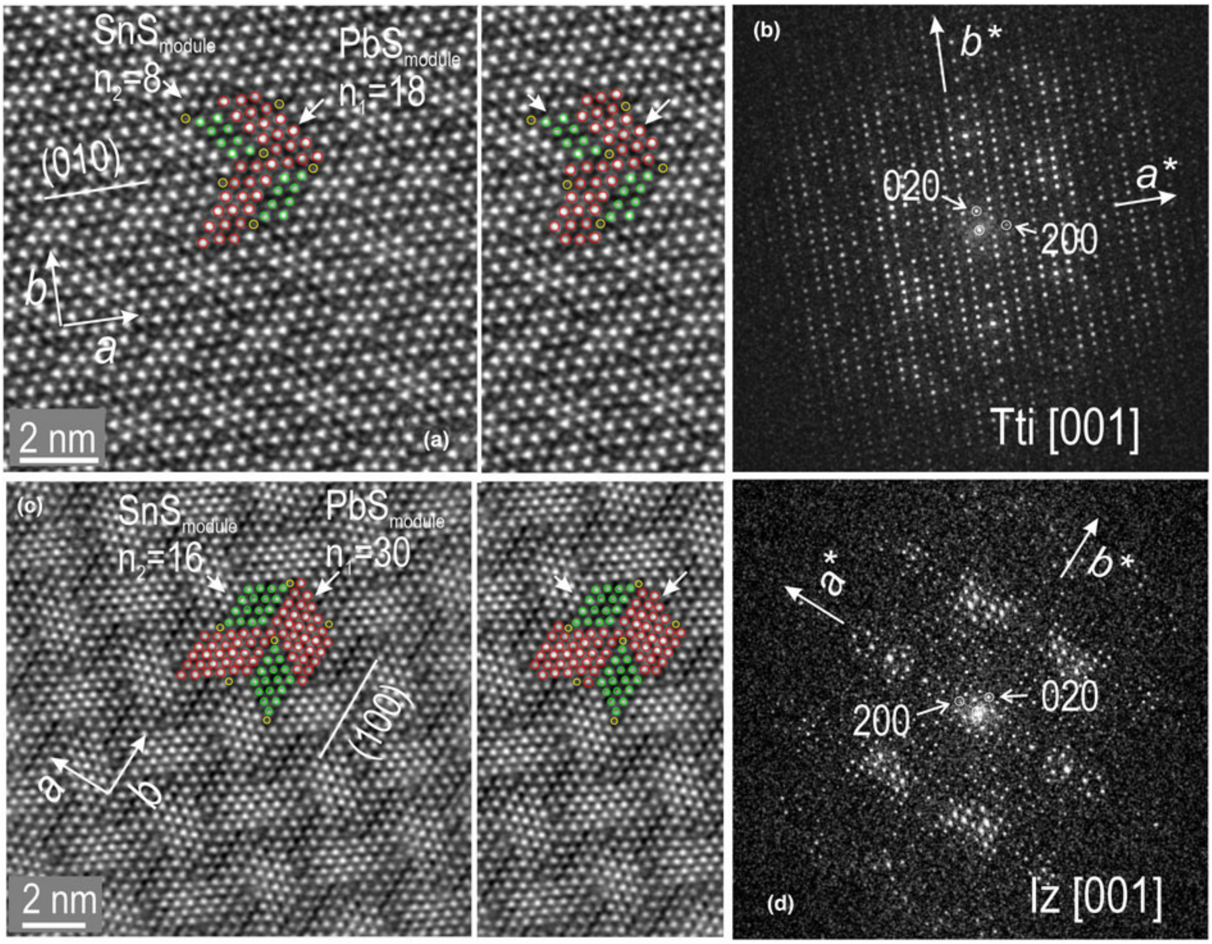

Figure 6. High-resolution HAADF STEM images and corresponding fast Fourier transform (FFT) patterns for tintinaite (Tti) and izoklakeite (Iz) on [001] zone axis (labelled in square brackets). The SnS ($n = 8$ and 16 for Tti and Iz) and PbS ($n = 18$ and 30 for Tti and Iz) building modules are shown as overlays (green and red, respectively) highlighting the number of bright dots corresponding to heavier atoms; less brighter atoms at the corners of the modules are shown in yellow. The modules are depicted in (a) and (c) use the approach of Li *et al.* (2019) on the left, and Makovicky and Mumme (1986) on the right.

adjustments along the (010$_{\text{Tti}}$ and (100)$_{\text{Iz}}$ planes (Fig. 10b,c). At higher magnification, the adjustments are illustrated by misorientations in the building modules (Fig. 10d) and swells along boundaries (Fig. 10e), as well as loops and kinks of the smallest-scale arrays of one species within another (Fig. 10f). Defects along (100) planes in izoklakeite show a doubling of the building modules and their displacements at the edges of the defects or along mutual contacts between the two sulfosalts (Fig. 10g,h).

The match between the values of b_{Kbl} and a_{Iz} at ~34 Å allows formation of intergrowths between tintinaite and izoklakeite (Fig. 11). The alternating PbS and SnS modules that form a zig-zag line along (100$_{\text{Tti}}$//(010)$_{\text{Iz}}$ planes are shown on the model in Fig. 11a. The change between tintinaite and izoklakeite along a_{Tti} and b_{Iz} is achieved by increasing the width of these modules whereas their heights remain constant (~17 Å). The HAADF STEM image shows a perfect match with the model (compare Fig. 11a and b). Oblique contacts between [001]$_{\text{Tti}}$ and [001]$_{\text{Iz}}$ are often observed (Fig. 11c). In this case the alignment between (010)$_{\text{Tti}}$ and (100)$_{\text{Iz}}$ planes features small-scale areas of mismatch, recognisable by misfit of the two types of modules and their respective morphologies (Fig. 11d,e). Formation of defects and nano- to micro-fractures are both associated with element remobilisation and accompany this type of low-angle misfit between the two sulfosalts (see below).

The second most common type of modular intergrowths within either tintinaite or izoklakeite is observed along planes from the <110> family (Fig. 12). Single arrays of smaller PbS modules along (1$\bar{1}$0) planes in izoklakeite (Fig. 12a) can be interpreted as modules corresponding to an $N = 3$ homologue (N3), i.e. from $n1 = 24$ and $n2 = 12$ defined by PbS and SnS modules, albeit with corner-sharing of atoms between PbS modules along (100)$_{\text{Iz}}$ (Fig. 12b). Arrays of thicker SnS modules along (1$\bar{1}$0) planes in tintinaite (Fig. 12c) can be interpreted as two PbS modules of the N3 homologue alternating with SnS modules of tintinaite (Fig. 12d). Likewise, module disorder and formation of the N3 homologue are observed when the intergrowths comprise changes in thickness or branching between arrays of different orientations (Fig. 12e–h).

A range of textures crosscutting the main crystal structural motifs of the two sulfosalts and leading to redistribution of Bi and Se are also depicted (Fig. 13). Modifications of the PbS module in both izoklakeite or tintinaite, e.g. giving them an S-shaped or irregular appearance, are present as single defects (Fig. 13a–c), or occur along nanofractures displaying Bi enrichment (Fig. 13d). Some lamellae (~26 Å-wide) feature building modules which, although syntactic with host tintinaite, are different to kobellite homologues (Fig. 13e). These are associated with localised enrichment in Bi and Se, and depletion in Sb (Fig. 13f).

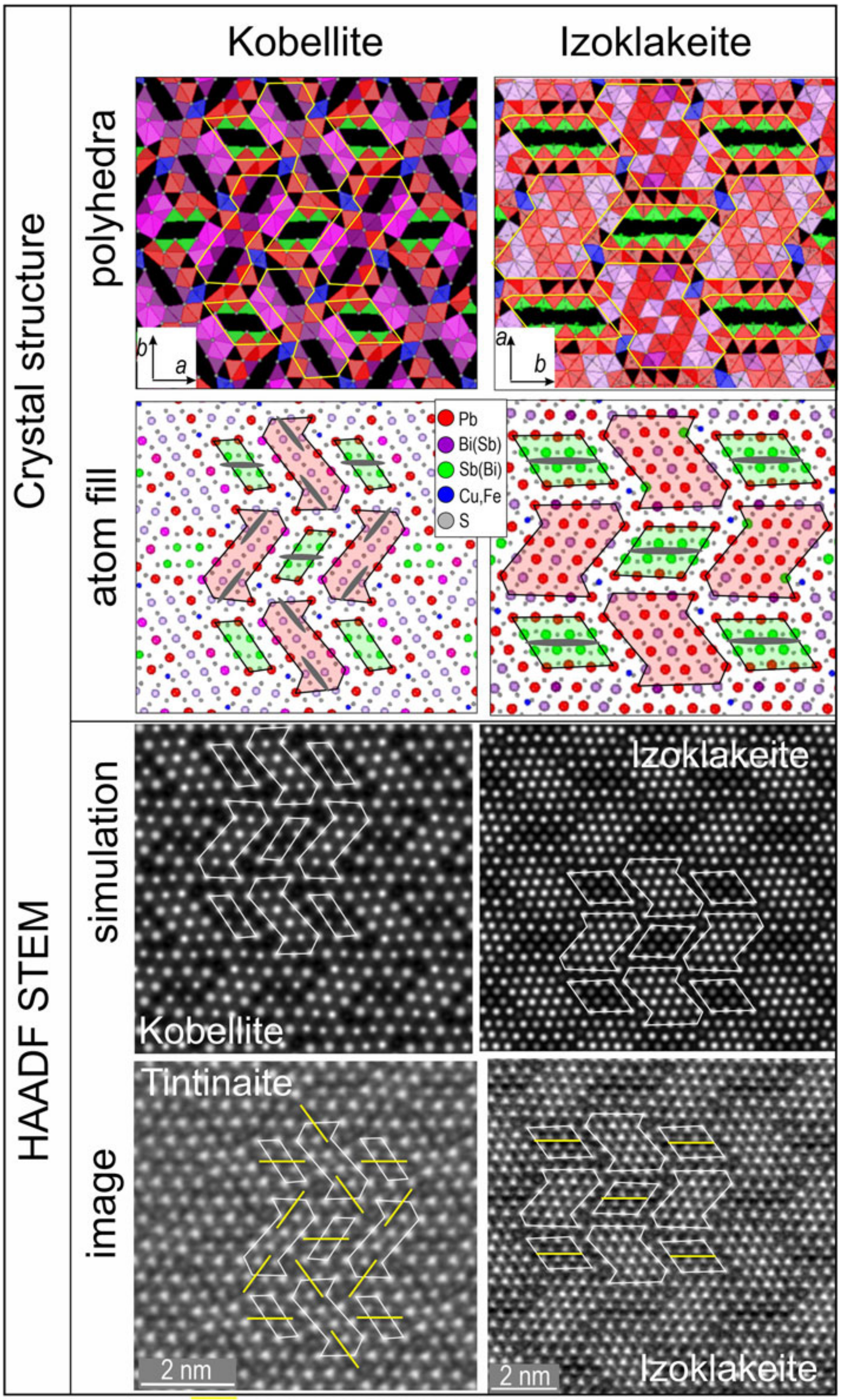

Figure 7. Crystal models, STEM simulations of kobellite and izoklakeite on [001] zone axis as labelled. Images for tintinaite and izoklakeite shown at the bottom of the figure. Simulations were obtained using the structures of Miehe (1971) and Makovicky and Mumme (1986) for kobellite and izoklakeite, respectively. The SnS and PbS building modules are highlighted by overlays. Weaker/longer Sb(Bi)–S bonds between adjacent polyhedra interpreted as lone electron pair micelles (e.g. Makovicky and Mumme, 1986) are marked by grey lines on atom-fill models. These correspond to dark lines on HAADF STEM images for tintinaite and izoklakeite and are highlighted by yellow lines across the overlays. Note that such features are visible through the middle of the SnS modules in izoklakeite, whereas in tintinaite they also occur through the PbS modules.

Discussion

Compositional variation in kobellite homologues: comparison with other occurrences

The compositional variation observed in species from the tintinaite–kobellite and izoklakeite–giessenite series from previously published studies spanning a range of magmatic–hydrothermal and metamorphosed deposits (Fig. 14; Supplementary Table S3) reflects the ability of modular structures to adapt to changes in physical and chemical parameters of fluids during ore formation.

The Boliden izoklakeite, $Iz_{\sim 60}Gie_{\sim 40}$, is richer in Sb (highest Iz component) than all previously published data (Table 1, 4 and Supplementary Table S3), including the type specimen from Izok Lake, Canada (Harris *et al.*, 1986) with composition $Iz_{53}Gie_{47}$.

Likewise, the average tintinaite composition, Tti $_{66}Kbl_{34}$, shows this is also rich in Sb, comparable to Pedra Luz, $Tt_{i65}Kbl_{35}$ (Moëlo

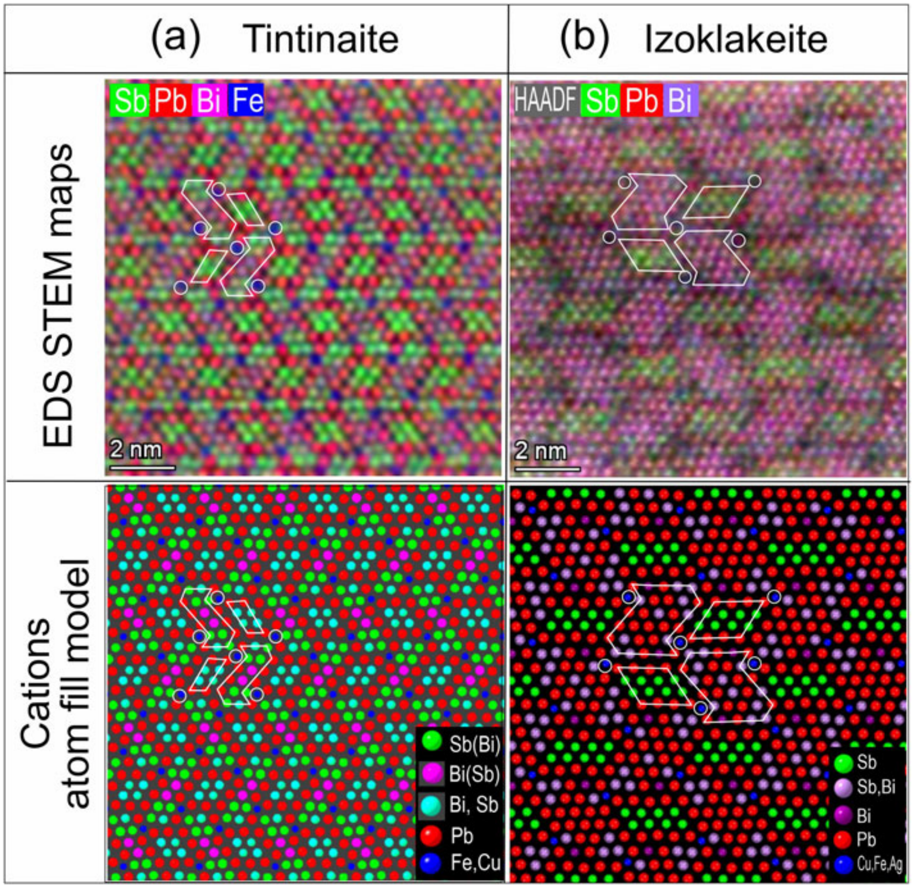

Figure 8. Atomic resolution map overlays and models for tintinaite$_{[001]}$ and izoklakeite$_{[001]}$ as labelled. Extended element-distribution maps and additional overlays for tintinaite and izoklakeite are shown in Supplementary Figs S2 and S3. Models were obtained using the structures of Miehe (1971) and Makovicky and Mumme (1986) for kobellite and izoklakeite, respectively. Note the match between the atomic arrangement and the building modules SnS and PbS shown as overlays. Circles show the atoms at the corners of these modules (Fe, Cu) and (Cu, Fe, Ag) for tintinaite and izoklakeite, respectively. Such atoms are exceptionally well depicted by the Fe maps for tintinaite.

et al., 1995), and higher than the $\mathrm{Tti_{51}Kbl_{39}}$ composition from Boliden given by Wagner and Jonsson (2001) (Tables 2, 4 and Supplementary Table S3). The Tti:Kbl ratio in tintinaite analysed here shows a Tti:Kbl range between 64:36 and 69:31, clearly representing the highest Sb-rich composition reported if we exclude the TL tintinaite which lacks any Bi (Harris *et al.*, 1986). Previously reported data for the $N = 2$ homologue considered kobellite from Boliden have Tti:Kbl ratios midway through the series, i.e. 50:50 (Moëlo *et al.*, 1984) and 52:48 (Mumme *et al.* (2013), highlighting the constraints of local conditions on compositional variation in a single deposit. All studies of the homologue $N = 2$ from Boliden, including the present data, affirm these are Se-rich specimens (~3–4 wt.%; Tables 2 and S3). The izoklakeite reported here from Boliden is also Se-rich (~5 wt.%; Table 1). The Se-rich environment from which these sulfosalts have formed is further emphasised by the presence of 2.81 wt.% Se in Bi-rich jamesonite (Table S4). Selenium-bearing assemblages of jamesonite and tintinaite are also reported from Úhorná, Spišsko Gemerské Rudohorie Mts., Slovakia (Pršek and Peterek, 2008). The Korunka Mine specimen used for refinement of the kobellite crystal structure (Miehe, 1971) is from the same sulfosalt rich, hydrothermal vein system (~1200 veins) in Eastern Slovakia as the Úhorná specimen. As at Boliden, we note that the Tti:Kbl ratio changes from 60:40 to 44:56, emphasising the presence of both tintinaite and kobellite in the same orefield.

Mirroring the Boliden kobellite homologues, distinct ranges of composition for the same sulfosalt within a given district or province are also reported (Moëlo *et al.*, 1995). At Boliden, co-crystallisation of the two sulfosalts is reflected by local variations in the Sb:Bi ratios in tintinaite throughout the three analysed areas in sample 1061a, i.e. the lowest ratio of 66:36 in area 2 when co-existing with izoklakeite, and highest (69:31) when co-existing with jamesonite in area 3 (Table 2).

The compositional data for the Boliden specimens (Tables 1–3) are compared in Fig. 14 with published data from other localities (list in Table 4) and ideal end-members for the two series (Supplementary Table S3, and references therein). The relative proportions of Pb, Bi and Sb, the three main elements in the *M* sites defining the structural modules for the two homologues, are depicted on the plot of Pb*/(Pb*+Bi+Sb–Ag) versus Bi/(Sb+Bi) where Pb* = (Pb+Ag+Cd+Zn) in Fig. 14. Locality details are given in Table 4.

Izoklakeite data separates into two groups: (i) 'Bi-rich izoklakeite' encompassing the specimen from Zervreila Lake, Switzerland (Armbruster and Hummel, 1987) and material from Gutaishan, China (Li *et al.*, 2019), and (ii) izoklakeite from the type locality (Harris *et al.*, 1986), Vena, Sweden (Zakrzewski and Makovicky, 1986) and the specimens from Boliden reported here. In addition to these, specimens from France and Portugal (Moëlo *et al.*, 1995) are defined from chemistry alone. Among these, Bazoges (France) includes both types of izoklakeite. Notably, Boliden izoklakeite plots at the lower end of the Bi/(Sb+Bi) range and within the central part ($x = 1$) of the $N = 4$ homologue band.

Specimens with greater Bi of homologue $N = 2$, kobellite *sensu stricto*, form a tight cluster with 0.55 > Bi/(Sb+Bi) > 0.7 including data from Korunka Mine (Miehe, 1971); Gutaishan (Li *et al.*, 2019); Vena, Sweden and Raleigh, USA (Moëlo *et al.*, 1984); Les Chalanches, France; and Pedra Luz, Portugal (Moëlo *et al.*, 1995). Two of the Boliden specimens at Bi/(Sb+Bi) ≈ 0.5 (Moëlo *et al.*, 1984; Mumme *et al.*, 2013) lie at the boundary

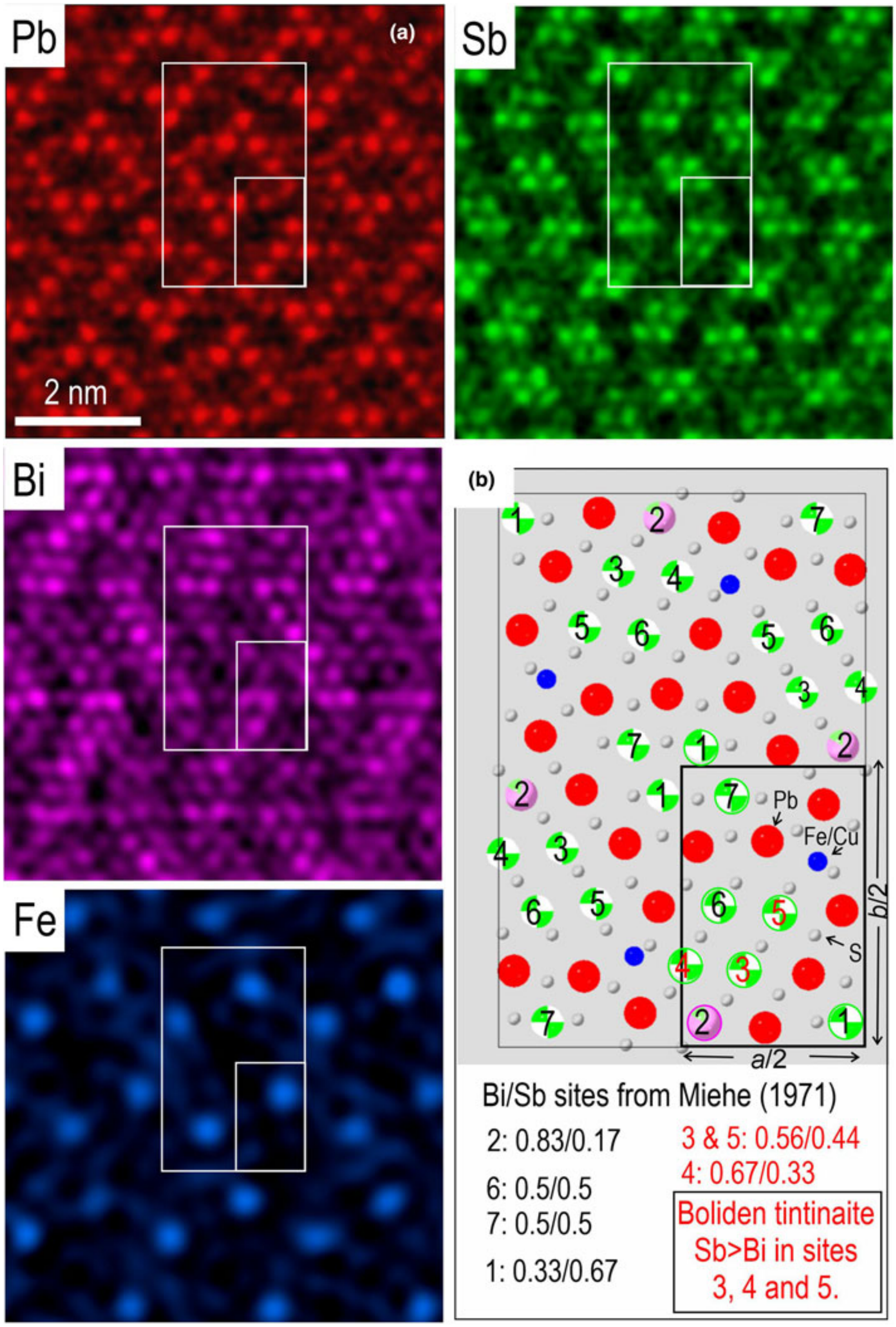

Figure 9. (a) Element-distribution maps for Pb, Sb, Bi and Fe in tintinaite (crops from maps in Supplementary Fig. S2) showing the distribution of these elements throughout the structure whereby four Bi/Sb sites lie at the centre of the SnS modules; these are surrounded by Pb atoms. (b) Crystal model for the asymmetric unit cell of kobellite from Miehe (1971), there are seven Bi/Sb sites (labelled by numbers) of which two have 0.5/0.5 ratios, whereas the others, except site #1 where Sb is twice as much as Bi (0.33/0.67), have occupancies in which Bi > Sb. The map for Sb suggests, however, that occupancy is Sb > Bi for sites #3, 4 and 5. This is in agreement with the higher Sb/(Sb+Bi) ratio in Boliden tintinaite compared with the kobellite specimen studied by Miehe (1971); 66 mol.% and 44 mol.% tintinaite, respectively.

between kobellite and tintinaite. The other tintinaite data include specimens from Rossland, Canada (Moëlo *et al.*, 1984), Pedra Luz (Moëlo *et al.*, 1995), Úhorná, Slovakia (Pršek and Peterek, 2008), data from Boliden (Wagner and Jonsson, 2001, and the present work, and the Sb-pure tintinaite from Tintina (Harris *et al.*, 1986; Moëlo *et al.*, 1984). The tintinaite–kobellite data plots along the middle to upper part of $N = 2$ band, with Korunka Mine kobellite at $x = 0$.

Primary nanoscale intergrowths: jigsaw patterns evolving from chessboard structures

Widespread nanoscale intergrowths between tintinaite and izoklakeite (Figs 3, 10–12) account for compositional fields in terms of M^{2+}(+Ag^{1+}) and M^{3+} cations when analysed at the micrometre-scale (Fig. 3). It is however interesting to note that the range of N values, 2.01–2.08 for tintinaite (Tables 2, 3) are slightly in excess of the ideal $N = 2$, whereas the range of N values for izoklakeite, 3.76–3.94 (Table 1) are in deficit relative to the ideal $N = 4$. This mirrors results for N values of kobellite homologues elsewhere (Table 4). Challenges in calculation of N values from EPMA data are introduced by excess of Cu over the 2 apfu in the tetrahedral site. In addition to Pb and (Sb,Bi) correction due to Ag incorporation (see above), attributing excess Cu to either Pb or (Sb,Bi) sites drives significant changes of N (Table 4; Fig. 14), as observed for kobellite from Raleigh (Moëlo *et al.*, 1984) and kobellite and izoklakeite from Les Chalanches (Moëlo *et al.*, 1984; 1995). The Bi-rich izoklakeite from

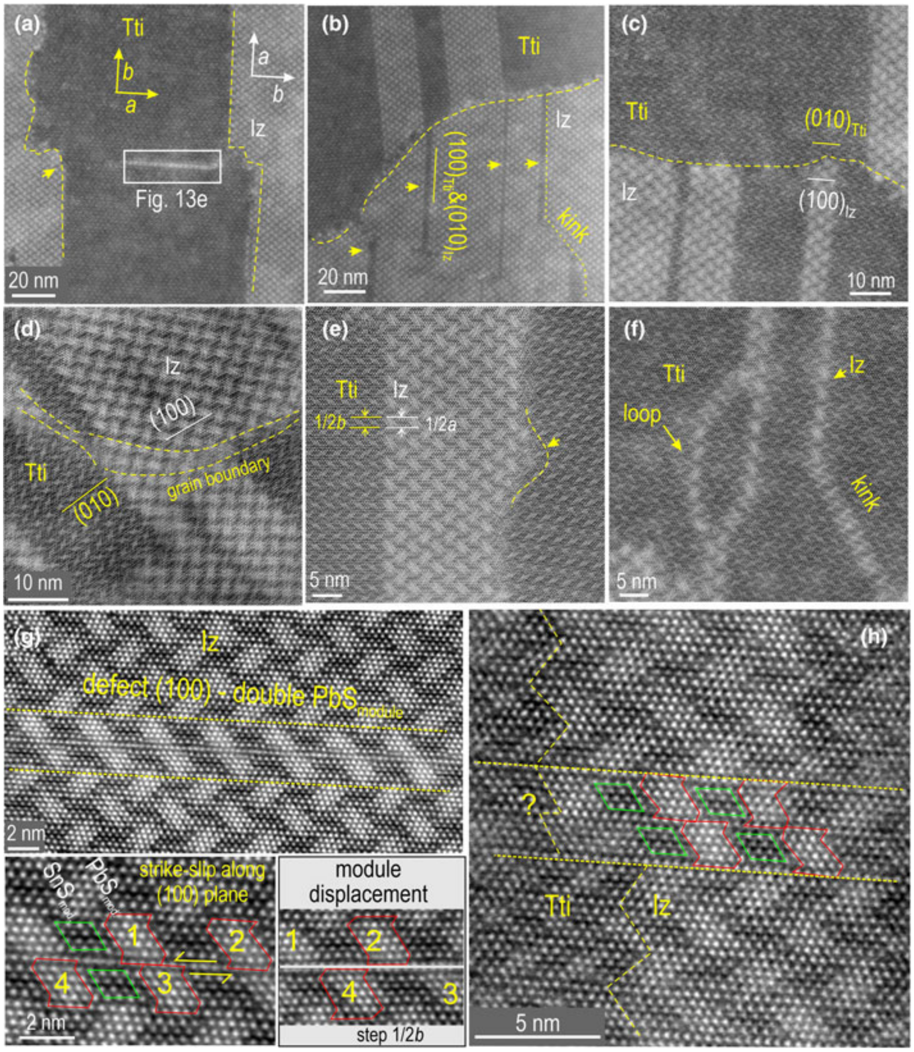

Figure 10. (a–f) Images showing various types of intergrowths between tintinaite (Tti) and izoklakeite (Iz). (a) Tintinaite lamella with straight and irregular contacts (arrowed). (b, c) Curvilinear interfaces between grains with lamellar intergrowths of different thickness. Direction of planes for boundaries and intergrowths given in brackets. (d, e) At higher magnification, the grain boundary adjustments (dashed line) are illustrated by misorientations in the building modules (in d) and swells along boundaries (in e). (f) Loops and kinks are common along smallest arrays of one sulfosalt into another, in this case izoklakeite within tintinaite. (g) Defect along (100) plane showing doubling of PbS modules in izoklakeite (image at the top). Underneath, left side, a detail showing the building modules (red outline for PbS, also numbered, and green for SnS) are shown to be displaced from one another along a strike-slip plane. At the edge (right side) of the defect, the displacement is by ½ *b* along the (100) plane. (h) Module displacement within izoklakeite affecting the contact with tintinaite.

Zervreila Lake (Armbruster and Hummel, 1987) gives $N = 4.08$ and 4.54, if Ag is incorporated within the (Sb,Bi) or Pb sites, respectively. The *N* excess of tintinaite, and *N* deficit of izoklakeite, may indicate that, at the scale of the electron probe spot, the analysed volume of each sulfosalt integrates a minor fraction of the other sulfosalt as a syntactic intergrowth.

Difficulties in attributing specific schemes of (Sb,Bi,Pb) ordering in izoklakeite that markedly differ in chemistry were discussed in detail by Armbruster and Hummel (1987) using the examples of Bi- and Sb-rich varieties from Lake Zervreila and Vena (Makovicky and Mumme, 1986). Although this does not affect the identification of building modules by HAADF STEM imaging of either Bi- or Sb-rich izoklakeite and kobellite and tintinaite, as shown for specimens from Gutaishan (Iz_{35} and Kbl_{61}; Li *et al.*, 2019) and Boliden (Iz_{60} and Tti_{60}; Figs 6, 7), it is nevertheless reflected in the atom-resolution mapping of izoklakeite and tintinaite (Fig. 8).

A novel feature of the sulfosalt intergrowths from Boliden are the SnS and PbS modules with $n = 12$ and 24, respectively, imaged as arrays of combined SnS and PbS modules in either izoklakeite or tintinaite (Fig. 12). These correspond to modules suggested for a hypothetical $N = 3$ member of the kobellite series (Makovicky and Mumme, 1986) with an estimated structural formula (without Ag) that can be given as: $(Cu_{2-x}Fe_x)Pb_{18+x}(Sb,Bi)_{18-x}S_{46}$. The structure of the $N = 3$ homologue is illustrated as Fig. 15.

Structural versatility of these sulfosalts is moreover reflected in the ability to combine modules corresponding to different homologues such as $SnS_{Tti=Kbl}$ and $PbS_{N=3}$. Other structures can be derived forming a broader family of Pb–Bi–Sb sulfosalts considered as kobellite homeotypes (Makovicky and Balić-Žunić, 2023, and references therein).

Structural arrangements in kobellite homologues have been described as ‘cyclically twinned’ (Makovicky, 1985), ‘boxwork’ (Makovicky, 1997), ‘chessboard’ (Li *et al.*, 2019) or quasi-chessboard (Makovicky and Balić-Žunić, 2023). Chessboard structures are highly adaptable to accommodating nanoscale intergrowths between modules of variable sizes and combinations of thereof (Figs 11, 12), leading to smallest scale 2D jigsaw-like patterns.

Such physical–chemical behaviour can be considered as a type of microstructural evolution in complex nonlinear systems, a topic of interest from both theoretical and engineering viewpoints. For instance, quasiperiodic two-phase nanowire chessboard structures are common in a variety of materials from decomposing alloys to oxide ceramics and have been modelled as tweed structures with an underlying chessboard feature evolving during pseudospinodal decomposition (Ni and Khachaturyan, 2009). Chessboard-like supramolecular structures on $Au_{(111)}$ surfaces designed for chemical functionalisation of bio-sensors and molecular electronics

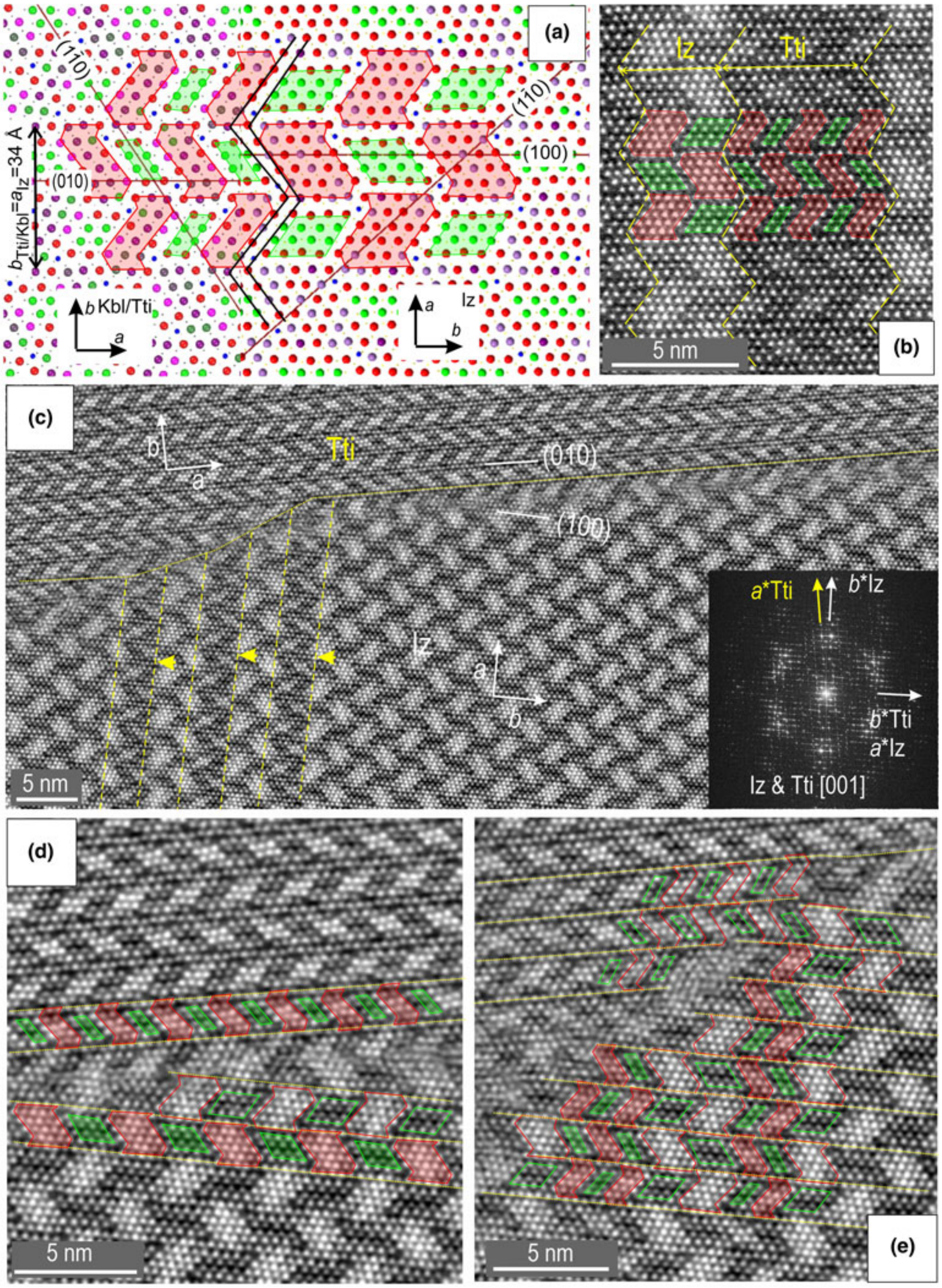

Figure 11. Schematic model (a) and image (b) showing coherent contacts between izoklakeite (Iz) and tintinaite (Tti). PbS and SnS building modules are shown as red and green overlays. The match between b_{Tti} and a_{Iz} features alternating PbS and SnS modules that form a zig-zag line. (c) An oblique contact between $[001]_{Tti}$ and $[001]_{Iz}$. Parallel arrays of tintinaite within izoklakeite are arrowed. The misalignment a^*_{Tti} and b^*_{Iz} is also shown in the FFT (inset). (d, e) Alignment between $(010)_{Tti}$ and $(100)_{Iz}$ planes features small-scale areas of mismatch, recognisable by misfit of the two types of modules and their respective morphologies.

(Dou *et al.*, 2015), or broadband chessboard surfaces with a double-layer for an electromagnetic gap band structure (Mighani and Dadashzadeh, 2016), are among materials with block modularity akin to those discussed here.

Lone electron pair micelles – depicting Sb-rich kobellite homologues

The wide variety of distorted polyhedra, ranging from six to nine-fold coordination environments, is the basis for crystal structural modularity shared by Pb–Bi–Sb-sulfosalts (Makovicky, 1997, and references therein). This is due to variable stereochemical activity of the lone electron pair of Pb^{2+}, Bi^{3+} and Sb^{3+} which, statistically, has a decreasing influence on distortion of the coordination polyhedra with increasing atom size Sb < Bi < Pb (Armbruster and Hummel, 1987). Makovicky and Mumme (1986) discussed the formation of lone electron pair micelles as a means to structurally accommodate stereochemical active pairs along interfaces in sulfosalts with reference to kobellite homologues. These concepts were subsequently taken to defining modularity in Pb–Sb-

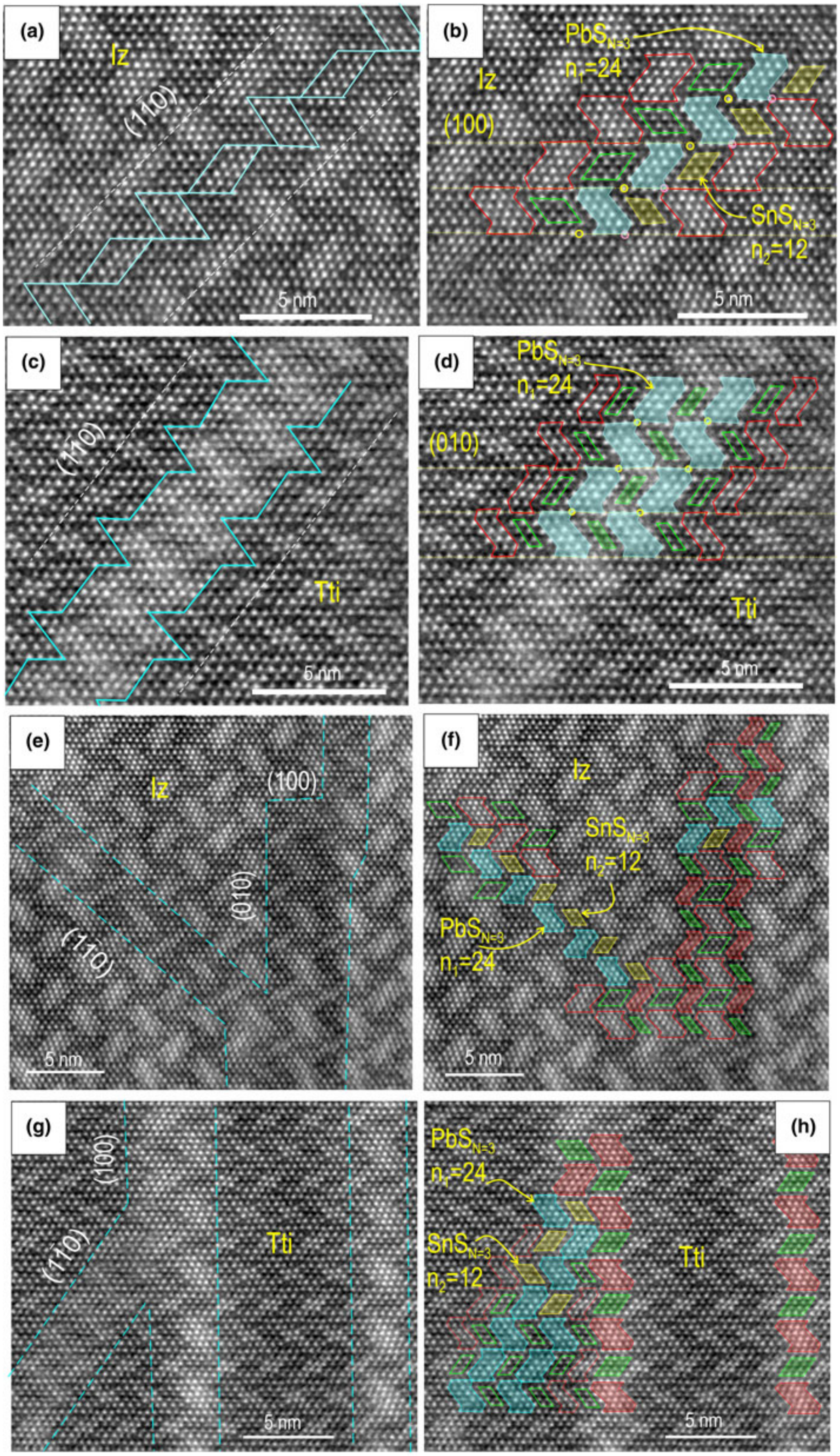

Figure 12. (a, d) Single and double arrays of modular intergrowths in izoklakeite (Iz) and tintinaite (Tti) along planes from the <110> family showing PbS ($n = 24$; blue) and SnS ($n = 12$; yellow) modules corresponding to the $N = 3$ homologue. Circles represent dots/atoms unaccounted for. (a, b) A single array (blue line in (a)) of the $N = 3$ homologue shown as PbS_{N3} (blue)–SnS_{N3} (yellow) modules within izoklakeite (PbS_{Iz} and SnS_{Iz} modules outlined in red and green). (c, d) A double array (blue line in (c)) of PbS_{N3} modules intergrown with SnS_{Tti} modules in tintinaite. (e–h) Module disorder involving slabs of $N = 3$ homologue in intergrowths comprising changes in thickness or branching between arrays of different orientations as labelled in izoklakeite and tintinaite.

sulfosalts based on the arrangement of micelles into ‘fish-bone’ zigzag layers (e.g. Moëlo *et al.*, 2000; Biagioni *et al.*, 2016).

An outstanding result of the present study is depiction of the dark line patterning through the middle of SnS modules on the HAADF STEM images of Sb-rich homologues (Figs 6, 7). These are attributable directly to the lone electron pair micelles in the structures, as outlined for example in izoklakeite (Makovicky and Mumme, 1986). Notably, these features were not identified on the HAADF STEM images of Bi-rich kobellite homologues from Gutaishan (Li *et al.*, 2019), and thus confirm the stronger influence

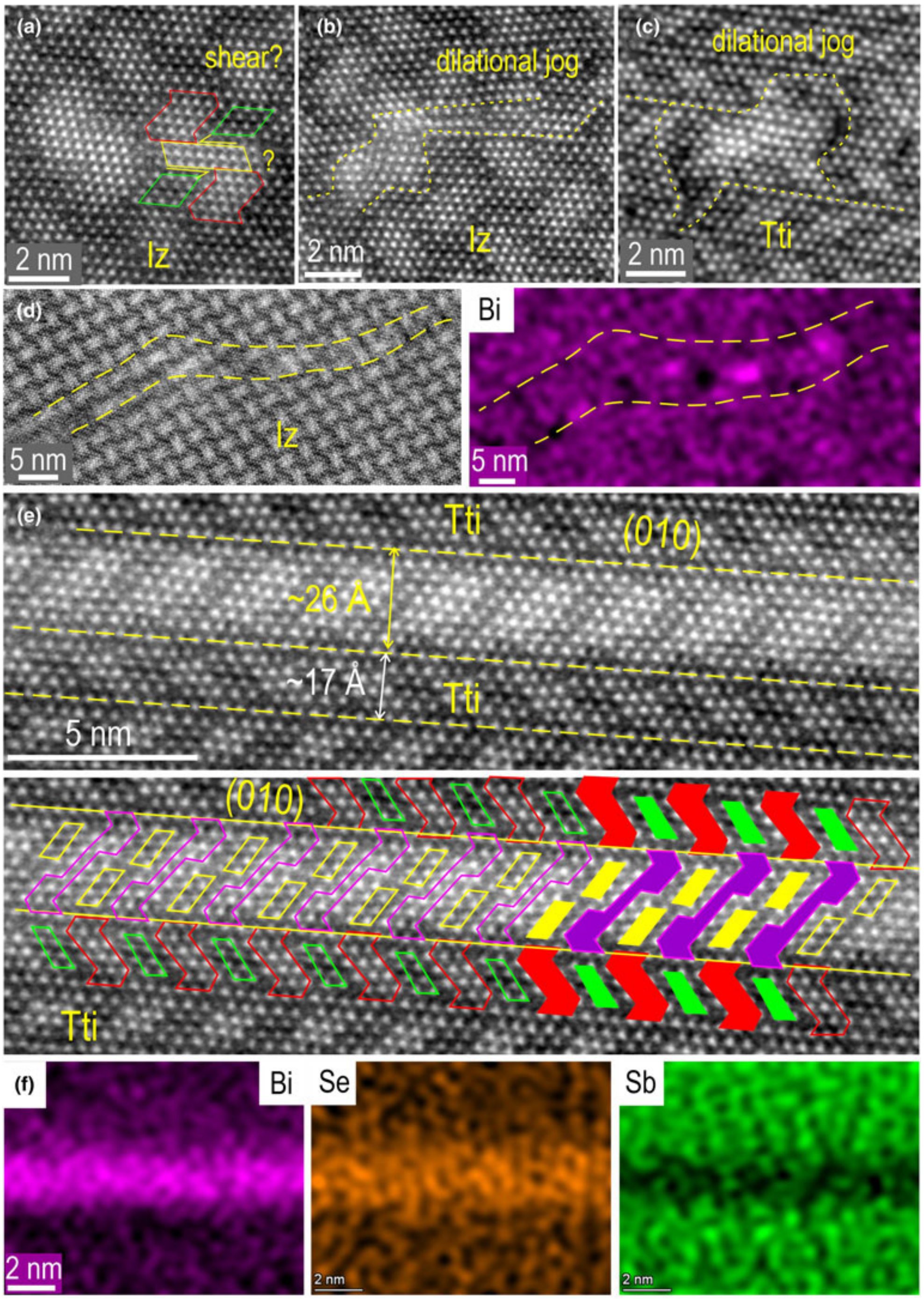

Figure 13. Defects and textures crosscutting the main crystal structural motifs of the two sulfosalts and leading to redistribution of Bi and Se in izoklakeite (Iz) and tintinaite (Tti). (a) S-shaped defect derived from modification of PbS modules (red outline) in izoklakeite attributable to shear–displacement along $(100)_{Iz}$ planes. SnS_{Iz} module outlined in green. Note a slab of $n = 24$ dots/atoms of equal intensity with the PbS_{Iz} along the displacement plane. (b, c) Defects showing irregular aggregation of PbS modules that are interpreted as dilational jogs in izoklakeite and tintinaite. (d) Nanoscale fracture in izoklakeite displaying Bi remobilisation. (e) Image showing a ∼26 Å-wide lamella featuring building modules, which, although syntactic with host tintinaite, are different to kobellite homologues. A possible interpretation of the modules along the lamellae are given as overlays underneath the image. The SnS and PbS modules in tintinaite are also shown as green and red overlays. (f) EDS STEM maps of image in (e) showing localised enrichment in Bi and Se, and depletion in Sb.

of Sb relative to Bi atoms in terms of stereochemical activity of the lone electron pair (Armbruster and Hummel, 1987).

Ultralow thermal conductivity is a material property linked to the effect of lone electron pair micelles in strengthening bond anharmonicity as assessed in a synthetic $MnPb_{16}Sb_{14}S_{38}$ sulfosalt (Dawahre *et al.*, 2020). This study acknowledged the lack of thermal transport behaviour studies of Pb–Sb-sulfosalts despite their significant potential in terms of technological applications, ranging from thermoelectric energy conversion to thermal barrier coatings (e.g. Dittrich *et al.*, 2009).

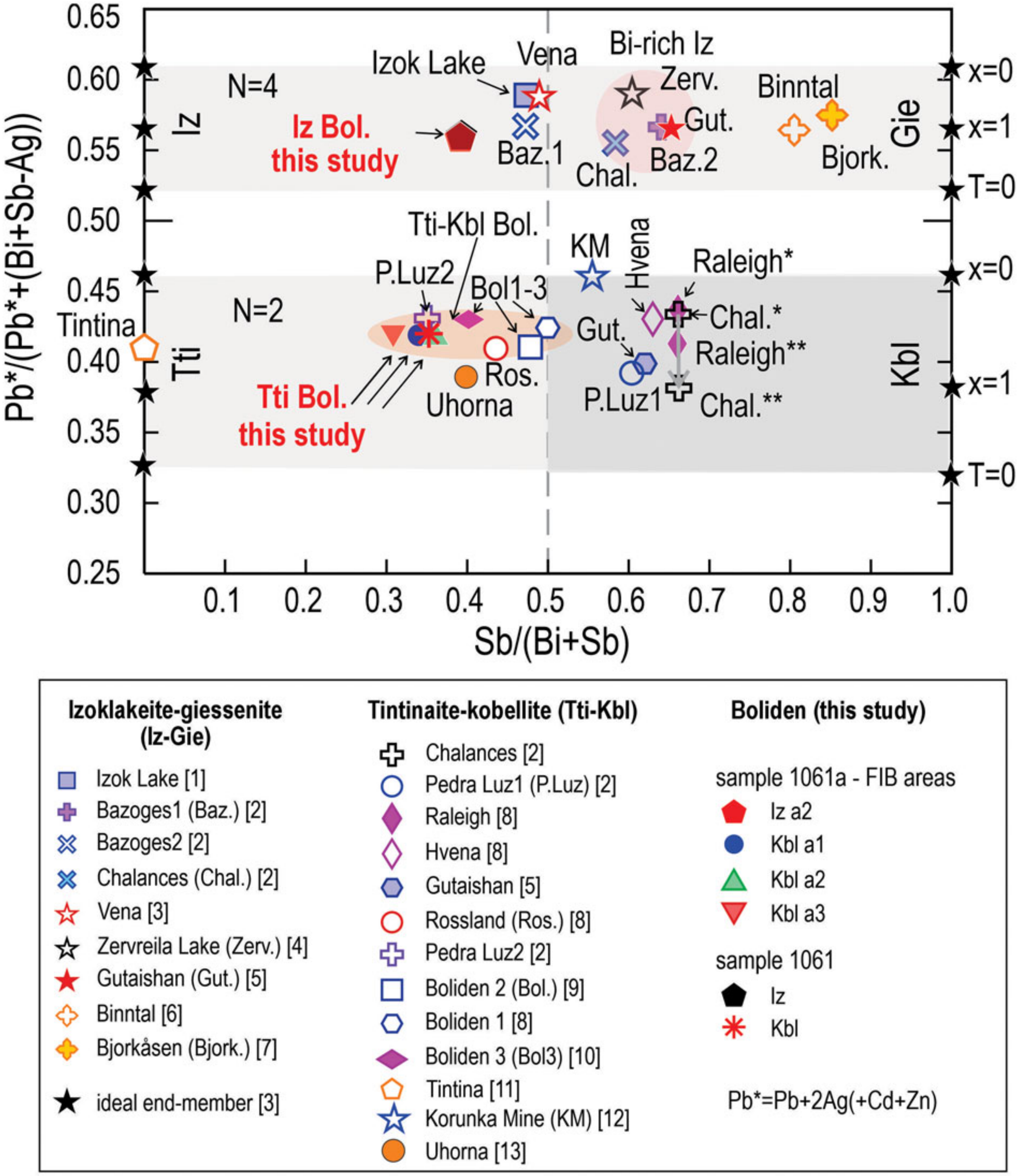

Figure 14. Diagram showing compositional variation in kobellite homologues from Boliden and comparison with other occurrences. Data from Tables 1–3 and Supplementary Table S3, References: [1] Harris *et al.* (1986); [2] Moëlo *et al.* (1995); [3] Zakrzewski and Makovicky (1986); [4] Armbruster and Hummel (1987); [5] Li *et al.* (2019); [6] Graeser and Harris (1986); [7] Makovicky and Karup–Møller (1986); [8] Moëlo *et al.* (1984); [9] Mumme *et al.* (2013); [10] Wagner and Jonson (2001); [11] Harris *et al.* (1968); [12] Miehe (1971); [13] Pršek and Peterek (2008). See text for further explanation and Table 4 for locality details.

Secondary textures; a record of metamorphic deformation

The range of shear, twist, jogs and displacement textures occurring as defects, crosscutting veinlets no more than a few nm wide, or along crystallographic planes in kobellite homologues (Figs 10g,h and 13) are secondary features attributable to superimposed syn-metamorphic deformation. These are associated with the redistribution of Bi and Se (Fig. 13f) and led to late formation of the Bi chalcogenides identified in areas of the samples bearing evidence of trace-element remobilisation at the micrometre scale (Fig. 2).

Such interpretations are concordant with assertions that sulfosalt-rich vein ores (containing kobellite homologues) experienced extensive ductile deformation post-dated by decomposition textures leading to formation of Se-rich assemblages (including

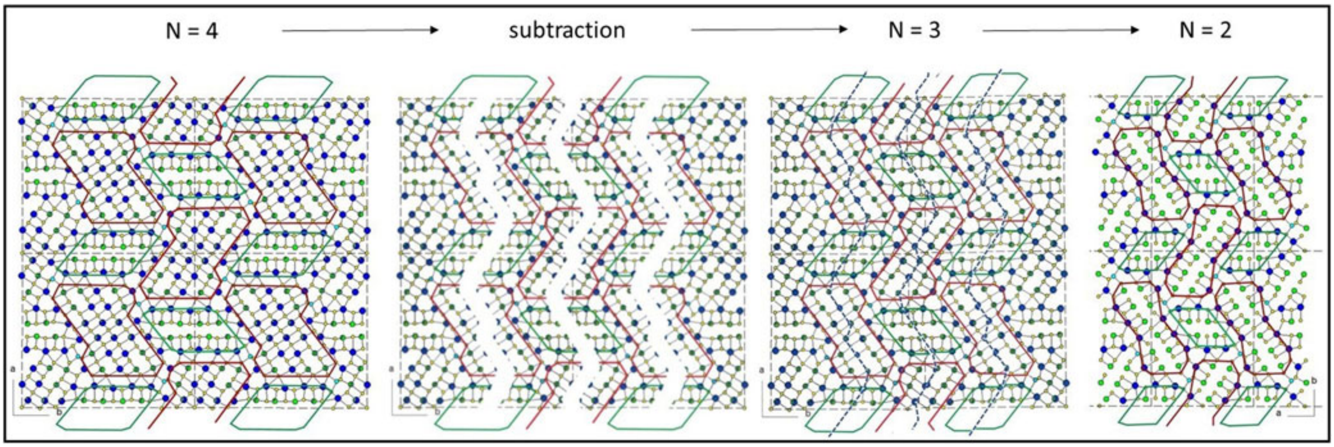

Figure 15. Proposed structure for the $N = 3$ homologue. The structural formula (without Ag) can be considered as $(Cu_{2-x}Fe_x)Pb_{18+x}(Sb,Bi)_{18-x}S_{46}$. Estimated unit cell parameters are $a = 34.1$ Å, $b = 41.5$ Å and $c = 4.05$ Å.

laitakarite) at Boliden (Wagner and Jonsson, 2001). The twists, shears and displacements of building modules or the low-angle imbrication boundaries in kobellite homologues resemble chain-width disorder in non-conventional pyriboles produced during syn-tectonic events (e.g. Konishi *et al.*, 2010; Campo-Rodriguez *et al.*, 2024). Twists and shears recorded by pyrite during brittle to ductile transition are among nanoscale textures associated with Au and accompanying trace element (re)mobilisation in brecciated ores (Ehrig *et al.*, 2023).

Summary and implications

The findings of the present study are summarised below.

(1) Sulfosalt assemblages from Boliden (Sweden) comprise micro- to nano-scale intergrowths of Se-rich izoklakeite ($Iz_{60}Gie_{40}$) and tintinaite (Tti_{66} Kbl_{34}) with average formulae and calculated homologue number (N) given as: $(Cu_{1.88}Fe_{0.18})_{\Sigma 2.06}(Pb_{22.92}Ag_{1.47}Cd_{0.01}Zn_{0.01})_{\Sigma 24.41}(Sb_{13.12}Bi_{8.69})_{\Sigma 21.8}(S_{50.19}Se_{6.43}Te_{0.12})_{\Sigma 56.73}$, $N = 3.83$, and $(Cu_{1.31}Fe_{0.74})_{\Sigma 2.05}(Pb_{10.58}Ag_{0.18}Cd_{0.05}Zn_{0.02})_{\Sigma 10.83}(Sb_{10.2}Bi_{5.23})_{\Sigma 15.43}(S_{32.22}Se_{2.46})_{\Sigma 34.7}$ and calculated $N = 2.05$, respectively. The two sulfosalts are also Se-rich, 4.83 wt.% and 3.3 wt.%, for izoklakeite and tintinaite.
(2) HAADF STEM imaging reveals chessboard structures comprising PbS and SnS building modules with the number of atoms (bright dots on images) in the octahedral (M) sites counted as: $n1 = 18$ and $n2 = 8$ for tintinaite, and $n1 = 30$ and $n2 = 16$ for izoklakeite. The homologue number can be calculated using the formula: $N = (n1/6) - 1$ and $N = n2/4$ for PbS and SnS modules giving $N_{Tti} = 2$ and $N_{Iz} = 4$.
(3) A new homologue, defined by $n = 12$ and 24 for SnS and PbS modules, corresponding to the $N = 3$ member of the kobellite series is identified as single or double units within areas with intergrowths between tintinaite and izoklakeite.
(4) HAADF STEM imaging of Sb-rich kobellite homologues reveals features attributable to lone electron pair micelles.
(5) The first atomic-resolution chemical mapping of Pb–Bi–Sb-sulfosalts shows a correlation with crystal structural modularity. The EDS STEM maps also highlight sites in the SnS modules of tintinaite in which Sb > Bi. Although this is only a qualitative assessment, the data is concordant with the overall Sb-rich composition of the Boliden specimen.
(6) Widespread coherent nanoscale intergrowths between kobellite homologues define jigsaw patterns evolving from chessboard structures and are considered to have formed during co-crystallisation of the two phases.
(7) A range of displacement textures and crosscutting veinlets (a few nm in width) are interpreted as evidence for superimposed syn-metamorphic deformation and are associated with the redistribution of Bi and Se.

Whereas crystal–structural modularity in Pb–Bi-sulfosalts is readily predictable from principles established some decades ago (Makovicky, 1997, and references therein), imaging and mapping using HAADF STEM techniques is a novel and ideally suited way to characterise such phases and their relationships down to the nanoscale (Ciobanu *et al.*, 2016). These tools hold untapped potential to unravel intricate pattern evolution of chessboard structures with applications across mineralogy but extending into allied fields of materials science and nanotechnology.

Acknowledgements. This work was funded by The University of Adelaide through a “Women’s Research Excellence Award” to C.L.C. and seed funding for nanoscale studies from BHP Olympic Dam. We appreciate the valuable comments and insights from Yves Moëlo, including his suggestion to include Fig. 15. We thank Stuart Mills for his editorial handling of the manuscript.

Supplementary material. The supplementary material for this article can be found at https://doi.org/10.1180/mgm.2024.41.

Competing interests. The authors declare none.

References

Armbruster T. and Hummel W. (1987) (Sb,Bi,Pb) ordering in sulfosalts: Crystal-structure refinement of a Bi-rich izoklakeite *American Mineralogist*, **72**, 821–831.

Biagioni C., Moëlo Y., Orlandi P. and Stanley C.J. (2016) Lead–antimony sulfosalts from Tuscany (Italy). XVII. Meerschautite, $(Ag,Cu)_{5.5}Pb_{42.4}(Sb,As)_{45.1}S_{112}O_{0.8}$, a new expanded derivative of owyheeite from the Pollone mine, Valdicastello Carducci: occurrence and crystal structure. *Mineralogical Magazine*, **80**, 675–690.

Campo-Rodriguez Y.T., Ciobanu C.L., Slattery A., Cook N.J., Schutesky M.E., Ehrig K., King S.A. and Yao J. (2024) Polysomatic intergrowths between amphiboles and non–classical pyriboles in magnetite: smallest–scale features recording a protracted geological history. *American Mineralogist*, **109**, 1798–1818.

Ciobanu C.L., Cook N.J., Pring A. and Green L. (2011) Focussed ion beam – transmission electron microscopy applications in ore mineralogy: bridging micron- and nanoscale observations. *Ore Geology Reviews*, **42**, 6–31.

Ciobanu C.L., Cook N.J., Maunders C., Wade B.P. and Ehrig K. (2016) Focused ion beam and advanced electron microscopy for minerals: insights and outlook from bismuth sulphosalts. *Minerals*, **6**, 112.

Dawahre L., Lu R., Djieutedjeu H., Lopez J., Bailey T.P., Buchanan B., Yin Z., Uher C. and Poudeu P.F.P. (2020) Lone-electron-pair micelles strengthen bond anharmonicity in $MnPb_{16}Sb_{14}S_{38}$ complex sulfosalt leading to ultralow thermal conductivity. *ACS Applied Materials and Interfaces*, **12**, 44991–44997.

Dittrich H., Stadler A., Topa D., Schimper H.-J. and Basch A. (2009) Progress in sulfosalt research. *Physica status solidi*, **206**, 1034–1041.

Dou R., Yang Y., Zhang P., Zhong D., Fuchs H., Wang Y. and Lifeng Chi (2015) Building chessboard-like supramolecular structures on Au(111) surfaces. *Nanotechnology*, **26**, 385601.

Ehrig K., Ciobanu C.L., Verdugo-Ihl M.R., Dmitrijeva M., Cook N.J. and Slattery A. (2023) Lifting the cloak of invisibility: Gold in pyrite from the Olympic Dam Cu–U–Au–Ag deposit, South Australia. *American Mineralogist*, **108**, 259–276.

Graeser S. and Harris D.D. (1986) Giessenite from Giessen near Binn, Switzerland: New data. *The Canadian Mineralogist*, **24**, 19–20.

Grip E. and Wirstam Å. (1970) The Boliden sulphide deposit. A review of geo-investigations carried out during the lifetime of the Boliden mine, Sweden (1924–1967). *Sveriges Geolokiska Undersökning*, C651.

Harris D.C., Jambor J.L., Lachance G.R. and Thorpe R.I. (1968) Tintinaite, the antimony analogue of kobellite. *The Canadian Mineralogist*, **9**, 371–382.

Harris D.C., Roberts A.C. and Criddle A.J. (1986) Izoklakeite, a new mineral species from Izok Lake, Northwest Territories. *The Canadian Mineralogist* **24**, 1–5.

Konishi H., Xu H. and Dymek R.F. (2010) High-resolution TEM study of jimthompsonite, chesterite, and chain-width disorder in Archean ultramafic rocks from Isua, West Greenland. *American Mineralogist*, **95**, 73–80.

Li W., Ciobanu C.L., Slattery A., Cook N.J., Liu W., Wade B.P. and Xie G.Q. (2019) Chessboard structures: Atom–scale imaging of homologs from the kobellite series. *American Mineralogist*, **104**, 459–462.

Makovicky E. (1985) Cyclically twinned sulphosalt structures and their approximate analogues. *Zeitschrift fur Kristallographie*, **173**, 1–23.

Makovicky E. (1997) Modular crystal chemistry of sulphosalts and other complex sulphides. Pp. 237–271 in: *Modular Aspects of Minerals* (S. Merlino, editor). European Mineralogical Union, Notes in Mineralogy 1.

Makovicky E. and Balić-Žunić T. (2023) On the homeotypes of kobellite. *Mineralogy and Petrology*, **117**, 209–217.

Makovicky E. and Karup-Møller S. (1986) New data on giessenite from the Bjørkåsen sulfide deposit at Otoften, northern Norway. *The Canadian Mineralogist*, **24**, 21–25.

Makovicky E. and Mumme W.G. (1986) The crystal structure of izoklakeite, $Pb_{51.3}Sb_{20.4}Bi_{19.5}Ag_{1.2}Cu_{2.9}Fe_{0.7}S_{114}$. The kobellite homologous series and its derivatives *Neues Jahrbuch für Mineralogie, Abhandlungen*, **153**, 121–145.

Makovicky E. and Nørrestam R. (1985) The crystal structure of jaskólskiite, $Cu_xPb_{2+x}(Sb,Bi)_{2-x}S_5$ ($x \sim 0.2$), a member of the meneghinite homologous series. *Zeitschrift für Kristallographie*, **171**, 179–194.

Miehe G. (1971) Crystal structure of kobellite. *Nature Physical Science*, **231**, 133–134.

Mighani M. and Dadashzadeh G. (2016) Broadband RCS reduction using a novel double layer chessboard AMC surface. *Electronics Letters*, **52**, 1253–1255.

Moëlo Y., Jambor J.L. and Harris D.C. (1984) Tintinaïte et sulfosels associés de Tintina (Yukon): Tintinaïte et sulfosels associés de Tintina (Yukon): la cristallochimie de la série de la kobellite. *The Canadian Mineralogist*, **22**, 219–226.

Moëlo Y., Roger D., Maurel-Palacin D., Marcoux E. and Laroussi A. (1995) Chemistry of some Pb–(Cu, Fe)–(Sb, Bi) sulfosalts from France and Portugal. Implications for the crystal chemistry of lead sulfosalts in the Cu-poor part of the Pb_2S_2–Cu_2S–Sb_2S_3–Bi_2S_3 system. *Mineralogy and Petrology*, **53**, 229–250.

Moëlo Y., Meerschaut A. Orlandi P. and Palvadeau P. (2000) Lead–antimony sulfosalts from Tuscany (Italy): II – Crystal structure of scainiite, $Pb_{14}Sb_{30}S_{54}O_5$, an expanded monoclinic derivative of $Ba_{12}Bi_{24}S_{48}$ hexagonal sub–type (zinkenite group). *European Journal of Mineralogy*, **12**, 835–846.

Moëlo Y., Makovicky E., Mozgova N.N., Jambor J.L., Cook N., Pring A., Paar W., Nickel E.H., Graeser S., Karup-Møller S., Balić-Žunić T., Mumme W.G., Vurro F., Topa D., Bindi L., Bente K. and Shimizu M. (2008) Sulfosalt systematics: a review. Report of the sulfosalt sub-committee of the IMA Commission on Ore Mineralogy. *European Journal of Mineralogy*, **20**, 7–46.

Mumme W.G., Gable R.W. and Wilson N. (2013) A crystal structure determination of (selenian) kobellite from the Boliden Mine, Sweden. *Neues Jahrbuch für Mineralogie, Abhandlungen*, **191**, 109–115.

Ni Y. and Khachaturyan A.G. (2009) From chessboard tweed to chessboard nanowire structure during pseudospinodal decomposition. *Nature Materials*, **8**, 410–414.

Niizeki N. and Buerger MJ (1957) The crystal structure of jamesonite, $FePb_4Sb_6S_{14}$. *Zeitschrift fur Kristallographie*, **109**, 161–183.

Nuffield E.W. (1948). Observations on kobellite. *University of Toronto Studies: VI. Geological Series*, **52**, 86–89.

Ödman O. (1941) Geology and ores of the Boliden deposit, Sweden. *Sveriges Geologiska Undersökning*, C438.

Pršek J. and Peterek D. (2008) Bi–Se–Te mineralization from Úhorná (Spišsko Gemerské Rudohorie Mts., Slovakia): A preliminary report. *Mineralogia*, **39**, 87–103.

Wagner T. and Jonsson E. (2001) Mineralogy of sulfosalt-rich vein-type ores, Boliden massive sulfide deposit, Skellefte district, northern Sweden. *The Canadian Mineralogist*, **39**, 855–872.

Wagner T., Klemd R., Wenzel T. and Mattsson B. (2007) Gold upgrading in metamorphosed massive sulfide ore deposits: Direct evidence from laser-–ablation–inductively coupled plasma–mass spectrometry analysis of invisible gold. *Geology*, **35**, 775–778.

Weihed J.B., Bergstrom U., Billstrom K. and Weihed P. (1996) Geology, tectonic setting, and origin of the Paleoproterozoic Boliden Au–Cu–As deposit, Skellefte district, northern Sweden. *Economic Geology*, **91**, 1073–1097.

Zakrzewski M.A. (1984) Jaskólskiite, a new Pb–Cu–Sb–Bi sulfosalt from the Vena Deposit, Sweden. *The Canadian Mineralogist*, **22**, 481–485.

Zakrzewski M.A. and Makovicky E. (1986) Izoklakeite from Vena, Sweden, and the kobellite homologous series. *The Canadian Mineralogist*, **24**, 7–18.